DLP 3D-Printed Mullite Ceramics for the Preparation of MOFs Functionalized Monoliths for CO2 Capture

ceramics

MDPI

*Article*

# DLP 3D-Printed Mullite Ceramics for the Preparation of MOFs Functionalized Monoliths for $CO_2$ Capture

**Arianna Bertero [1], Bartolomeo Coppola [1], Yurii Milovanov [1,*], Paola Palmero [1], Julien Schmitt [2] and Jean-Marc Tulliani [1]**

[1] Politecnico di Torino, Department of Applied Science and Technology, INSTM R.U. Lince, 10129 Torino, Italy; arianna.bertero@polito.it (A.B.); bartolomeo.coppola@polito.it (B.C.); jeanmarc.tulliani@polito.it (J.-M.T.)
[2] Institut Charles Gerhardt, UMR 5253 Pôle Chimie Balard Recherche, 34293 Montpellier Cedex 5, France; julien.schmitt@umontpellier.fr
* Correspondence: yurii.milovanov@polito.it

**Abstract:** The aim of this work is to compare the traditional uniaxial pressing with an innovative shaping technique, Digital Light Processing (DLP), in the preparation of porous mullite ($3Al_2O_3{\cdot}2SiO_2$) supports to be functionalized with an active coating for $CO_2$ capture. Indeed, the fabrication of complex geometries with 3D-printing technologies allows the production of application-targeted solid sorbents with increased potentialities. Therefore, this research focused on the effect of the purity of the selected raw materials and of the microstructural porosity of 3D-printed ceramic substrates on the Metal Organic Frameworks (MOFs) coating efficiency. Two commercial mullite powders (Mc and Mf) differing in particle size distribution ($D_{50}$ of 9.19 µm and 4.38 µm, respectively) and iron oxide content (0.67% and 0.38%) were characterized and used to produce the substrates, after ball-milling and calcination. Mc and Mf slurries were prepared with 69 wt% of solid loading and 5 wt% of dispersant: both show rheological behavior suitable for DLP and good printability. DLP 3D-printed and pressed pellets were sintered at three different temperatures: 1350 °C, 1400 °C and 1450 °C. Mf 3D-printed samples show slightly lower geometrical and Archimedes densities, compared to Mc pellets, probably due to the presence of lower $Fe_2O_3$ amounts and its effect as sintering aid. Mullite substrates were then successfully functionalized with HKUST-1 crystals by a two-step solvothermal synthesis process. Ceramic substrate porosity, depending on the shaping technique and opportunely tuned controlling the sintering temperature, was correlated with the functionalization efficiency in terms of MOFs deposition. Three-dimensional-printed substrates exhibit a higher and more homogeneous HKUST-1 uptake compared to the pressed pellets as DLP introduces desirable porosities able to enhance the functionalization. Therefore, this work provides preliminary guidelines to improve MOFs coating on mullite surfaces for $CO_2$ capture applications, by opportunely tuning the substrate porosity.

**Keywords:** ceramics additive manufacturing; digital light processing; $CO_2$ capture; metal organic frameworks; mullite; porous ceramics; sintering temperature



**Citation:** Bertero, A.; Coppola, B.; Milovanov, Y.; Palmero, P.; Schmitt, J.; Tulliani, J.-M. DLP 3D-Printed Mullite Ceramics for the Preparation of MOFs Functionalized Monoliths for $CO_2$ Capture. *Ceramics* **2024**, *7*, 1810–1835. https://doi.org/10.3390/ceramics7040114

Academic Editor: Enrico Bernardo

Received: 4 October 2024
Revised: 20 November 2024
Accepted: 21 November 2024
Published: 29 November 2024



## 1. Introduction

Additive Manufacturing (AM) of ceramics can provide a valid alternative strategy to traditional shaping processes, additively forming 3D ceramic components layer-by-layer on the base of 3D model data. Implementation of AM technologies in the ceramic field has been much slower than for metals or polymers due to several challenges related to poor resolution, surface quality, mechanical properties, and scalability [1]. Nevertheless, AM can provide interesting advantages for ceramics production. [1–4]. The design freedom makes ceramics AM interesting for many applications, such as in the biomedical field (for bone tissue engineering [5–7] or dental restoration [5,8]), aerospace (e.g., aerospike nozzles [9], SiC optical mirrors [10]), or for energy and environmental aims (monolithic

SOFCs [11], sensors [12], piezoelectric materials [13], catalytic converters (CCs) [14–16]). Among AM processes, Digital Light Processing (DLP) offers the possibility to reach superior surface quality and dimensional precision, thus is reliable to produce ceramic complex structures with high resolution [17–19]. DLP is included into the vat-photopolymerization category, where ceramics bodies are obtained from a photosensitive ceramic slurry, cured layer-by-layer using a UV light [18,19]. In particular, the fine control over the geometry opens the possibility of an accurate fabrication of ceramic porous architectures, interesting as lightweight structures, biomimetic scaffolds, filters, etc. [20,21]. In this frame, DLP is a promising strategy for Carbon Capture and Storage (CCS) systems. Among the strategies proposed to limit climate change negative impacts and Green House Gas atmospheric concentration, according to the Sustainable Development Scenario (SDS) CCS is estimated to contribute up to 15% of the cumulative reduction in emissions [22]. Thus, nowadays the development of efficient CCS systems is a hot topic.

Several materials that interact with and capture $CO_2$ have been used as active sites for CCS. By now, the most common strategy applied at the industrial scale is amine chemical adsorption because of its high $CO_2$ capture efficiency. However, this solution does not allow overcoming crucial undesired limitations such as the employment of a large amount of sorbent, the high energy consumption and corrosiveness [23]. Thus, new solid $CO_2$ adsorbers are being investigated. Among the most promising microporous materials, Metal Organic Frameworks (MOFs) show great potential for CCS. MOFs seem preferable to the well-known zeolites and activated carbons due to their higher porosity and $CO_2$ uptake capacity [24–26]. Furthermore, their strong 3D network may ensure increased $CO_2$ selectivity, especially towards $N_2$ [23,27]. Their hybrid interconnected and crystalline structure consists of metal-based ions (e.g., $Cu^{2+}$, $Zn^{2+}$, $Al^{3+}$, $Cr^{3+}$) bridged by organic linkers, usually coordination polymers with specific functional groups (e.g., carboxylate, pyridyl). These microporous hybrid materials not only have a strong chemical and thermal stability but are especially very interesting because of their high specific surface area (some of them reaching 6000 $m^2\ g^{-1}$), and their opened structure, characterized by high porosity volume (up to 90%) and low density (from 0.21 to 1.00 $g{\cdot}cm^{-3}$) [23,24,27]. In particular, in the current work the use of HKUST-1 ($Cu_3(BTC)_2$, copper-1,3,5-benzene tricarboxylate), also called Cu-BTC or MOF-199, is proposed for CCS. Its advantages in terms of high microporosity and specific surface area (up to 2000 $m^2/g$ [24,25,28–35]), are well known in the literature and make it desirable for gas adsorption technologies, and especially for $CO_2$ capture applications [36–39].

Despite their desirable properties, the direct use of MOFs in gas adsorption implies serious drawbacks typical of powder bed systems: such as high pressure drops, affecting the mass transfer rate and the efficiency of the system, as well as poor handling which does not guarantee a good recyclability [40]. To solve these issues, novel CCS systems require highly porous substrates, usually coated with a microporous layer able to interact selectively with the desired species. The employment of different types of supports for MOFs coating have been investigated [41–48]. Porous ceramics are interestingly suitable since they provide strength to the structure, together with physical, chemical and thermal stability, and low thermal expansion. The substrate geometry is crucial since it should have a highly interconnected and porous channel allowing gas phase to diffuse within the system; at the same time, a high surface to volume ratio is required to enhance the contact between the active coating and the selective gas species to entrap [14,49–54]. Mullite ($3Al_2O_3{\cdot}2SiO_2$) is here selected as an ideal material for the 3D-printed substrates since it is a desirable refractory ceramic commonly used to realize porous supports thanks to its well-known properties (high mechanical strength, creep resistance, durability, low thermal expansion, and high thermal shock resistance [55–58]). Finally, it was demonstrated that mullite can be successfully shaped by DLP technique realizing complex architectures, tuning their permeability and porosity [12,47,59–63].

Despite previous studies about MOFs functionalization of ceramic substrates are reported in the literature [43,64], by now a simple and efficient method to produce well

adherent, homogeneous and mechanically stable MOFs coating on supports, which can improve the adsorption capacity respect to the respective powder bed, is still needed. One of the main challenges, is to enhance the weight fraction of the adsorbent microporous material adherent to the substrate to consequently scale up the $CO_2$ uptake. A promising strategy to synthetize a continuous coating on a support seems direct liquid hydrothermal synthesis [65] immersing the substrate in a liquid precursor solution and synthetizing MOFs under autogenous pressure, or MOFs crystals deposition on the support.

We previously developed new CCS by combining DLP of mullite with complex architecture and HKUST-1 coating by liquid hydrothermal synthesis [47]. We showed promising $CO_2$ capture properties of these materials thanks to the presence of a fine layer of HKUST-1 at the surface of the material. However, the CCS capacity is directly related to the amount of HKUST-1 coated on the material. A challenging goal is hence to increase the amount of MOF deposited on the substrate, which require tailoring MOFs interaction with ceramic. With this aim several methods were recently investigated, such as chemical treatment of the substrate [48] or surface modification with functional groups [66,67] but they have the drawbacks to introduce additional chemical treatment on the substrate. In this paper, we propose a novel strategy to enhance HKUST-1 mass coated on the ceramic substrate, by tuning the residual substrate micro- and nano-porosity. The surface roughness and porosity promote MOFs adhesion, and they can be easily increased without chemically modifying the substrate but by accurately choosing the shaping process and controlling the sintering temperature.

## 2. Experimental

### *2.1. Fabrication of Ceramic Substrates*

#### 2.1.1. Mullite Powder Characterization

To fabricate the ceramic substrates, two commercial mullite powders ($3Al_2O_3{\cdot}2SiO_2$) were used: ITOCHU MM (by ITOCHU CERATECH CORP, Aichi, Japan) and JMS-70 (produced by Jiangsu Jingxin New Material Co., Zhenwu Town, Jiangdu District, Yangzhou City, Jiangsu Province, China). Materials were kindly supplied by Saint-Gobain Research Provence (Cavaillon, France). Both mullite powders have been produced by sintering from high purity starting materials including industrial alumina and kaolin [68,69]. Such obtained mullite powders, are characterized by average particle size ($D_{50}$) values of 6.6 µm (JMS-70) and 12.8 µm (ITOCHU MM), as determined by laser granulometry (Mastersizer 3000, Malvern Pan'alytical, Worcestershire, UK). For the sake of clarity, from now on, the two mullite powders are distinguished on the base of their different granulometry and thus indicated as Mc (coarse for ITOCHU MM powder) and Mf (fine for JMS-70 powder).

Magnesium nitrate hexahydrate ($Mg(NO_3)_2{\cdot}6H_2O$ (99.0% purity, supplied by Sigma-Aldrich, St. Louis, MO, USA) was added to the mullite powders as a sintering aid at a 1 wt% ratio [70]. Each powder was mixed with the sintering additive and ball-milled for 48 h to decrease the grain size and to obtain a narrow particle size distribution. Table 1 shows the proportions used in the ball-milling step. Then, the ball-milled powders were calcined at 650 °C for 1 h (10 °C/min heating ramp) to obtain magnesium oxide from the thermal decomposition of $Mg(NO_3)_2{\cdot}6H_2O$ [71].

**Table 1.** Ball-milling conditions. Ratios are given in weight.

| | |
|---|---|
| Mullite [g] | 150 |
| MgO: mullite | 1:99 |
| Zirconia spheres: mullite | 6:1 |
| Water: mullite | 2:1 |
| Optimal rotational speed [rpm] | 84 |

Powder morphology was characterized using the Field Emission Scanning Electron Microscope (FESEM) Hitachi S4000 (Hitachi, Tokyo, Japan). All the characterizations were performed for the as-received, ball-milled and calcined forms.

The phase composition of the powders and sintered samples was determined by X-Ray Diffraction (XRD, Malvern Pan'alytical, Worcestershire, UK) with CuKα radiation (λ = 0.154056 nm) in the 2θ range 5–70°. A time per step of 22.95 s and step size of 0.0066° were used. The chemical compositions of the as-received, ball-milled and calcined powders were quantitatively investigated using a Rigaku Supermini 2000 X-ray fluorescence spectrometer (by Rigaku, Tokyo, Japan). Samples for XRF spectrometry were prepared inserting 7 g of mullite powder and 6 wt% of polyvinyl alcohol in aluminum compressible PelletCups® by Chemplex Industries (Palm city, FL, USA) with a diameter of 31.0 mm and 8.5 mm height; samples were uniaxially pressed for 1 min at 12 ton using a Manual Hydraulic Press (15 Ton) by Specac (Orpington, UK).

#### 2.1.2. Mullite Pressed Samples

Mc and Mf ball-milled powders were used to produce pressed samples using a manual hydraulic press by Specac. Pellets (green diameter of 13 mm and height ≈ 3 mm) and bars (green dimensions ≈ 17 × 3 × 5 $mm^3$) were shaped by uniaxially pressing ball-milled and calcined powders for 10 s at 220 MPa. The sinterability was investigated by dilatometric analysis (Netzsch Geraetebau GmbH 402E, Selb, Germany) performed on 3D-printed and pressed bars, up to 1550 °C, at the heating rate of 10 °C/min. On the basis of this analysis, some temperatures were selected, and pellets sintered at 1350 °C, 1400 °C, 1450 °C and 1550 °C without dwelling time, using a heating ramp of 10 °C/min (Figure 1a). The geometrical density ρ (g/$cm^3$) of green and sintered ceramics was determined by mass and geometric measurements. The density of the sintered samples was also determined by buoyancy method, following Archimedes' principle (Density Determination Kit, Sartorius YDK01, Göttingen, Germany). These sintered densities were then related to the theoretical density (TD) of mullite (3.17 g/$cm^3$ [70]). Mercury intrusion porosimetry (MIP) (Micromeritics Autopore V by Micromeritics Instrument Corporation, Norcross, GA, USA) was used to determine the macroporosity.

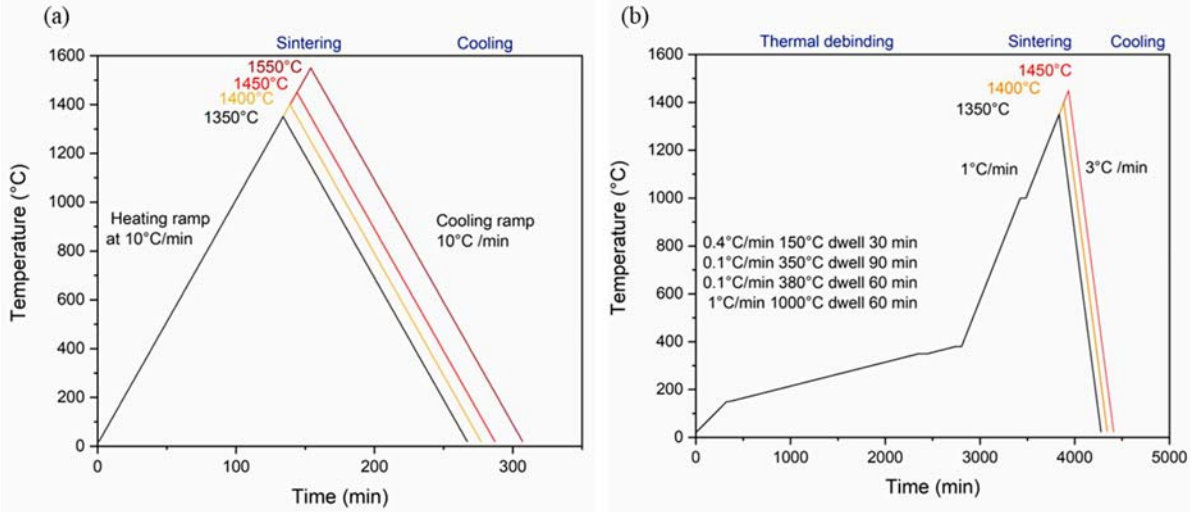


**Figure 1.** Schematic diagram of thermal cycles for pressed (**a**) and 3D-printed (**b**) pellets.

#### 2.1.3. Mullite 3D-Printed Samples

Two different ceramic photocurable slurries were prepared using Mc and Mf mullite powders with a photosensitive commercial resin (Admatec Europe BV, Alkmaar, The Netherlands) consisting of acrylates-based monomers containing the photoinitiator diphenyl(2,4,6-trimethylbenzoyl) phosphine oxide (TPO). A commercial dispersant

(Disperbyk-103, BYK Chemie, Wesel, Germany) was used to improve slurries stability while reaching high solid loading and keeping the viscosity low.

A ceramic slurry with a solid loading of 69 wt% of mullite powder (42 vol%) and 5.0 wt% of dispersant was obtained by mechanical mixing, following our previously established procedure [47]. For this work, Mc and Mf mullite powders were used, after ball-milling and calcination. Slurries were homogenized in agate jars with agate spheres (d = 10 mm) for 6 h at 350 rpm in a planetary miller (Fritsch Pulverisette, Fritsch GmbH, Idar-Oberstein, Germany). Before printing, air bubbles were removed from the slurries with 30 min degassing under vacuum using a rotary pump.

The slurries' rheological behaviors were analyzed at 25 °C with a rotational rheometer (Kinexus Pro+, Netzsch Gerätebau GmbH, Selb, Germany), at shear rates ranging between 0.1–1000 $s^{-1}$, equipped with stainless steel parallel plates (20 mm diameter), with a 1 mm gap between plates.

Pellets with a nominal diameter and height of 10 mm and 2 mm, respectively, were additively manufactured. A DLP-based stereolithographic printer was used (Admaflex 130, Admatec Europe BV, Alkmaar, The Netherlands): it operates with a 405 nm wavelength UV light. The slurry was spread on a moving tape through a 125 µm doctor blade. The curing depth was determined exposing slurries to UV light for different exposure times. The cured layers in a chessboard configuration were cleaned with paper to remove the uncured slurry and the thickness of the single layer was measured with a digital micrometer. After several tests, the curing parameters were optimized in order to provide the best compromise between high resolution, good adhesion, and uniformity of each layer. Therefore, a layer thickness of 30 µm was set. After an accurate printing parameter optimization, the chosen conditions were 2.5 s and 1.5 s as exposure times and 26.23 and 17.41 mW/$cm^2$ as LED power for Mc and Mf mullite slurries, respectively. A delay of 20 s before exposure was applied to let air bubbles be removed from the slurry. The .stl files were designed by AutoCAD 2018 software (Autodesk, San Francisco, CA, USA). As-printed bodies were firstly submitted to a water debinding process for 4 h at 30 °C, to easily remove the uncured slurry as well as the hydro-soluble components of the resin and then left overnight at room temperature. Subsequently, printed samples were oven-dried at 70 °C overnight before being submitted to thermal debinding and sintering processes, according to the treatment displayed in Figure 1b. Thermal treatments were performed in an electric furnace (Nabertherm, Nabertherm GmbH, Lilienthal, Germany) under air atmosphere. A slow heat treatment up to 400 °C aimed to avoid crack formation during resin decomposition. Since the reference pressed pellets exhibited a minimal residual porosity at a sintering temperature of 1550 °C, the printed samples were sintered only at the lower temperatures of 1350 °C, 1400 °C and 1450 °C, as shown in Figure 1b.

As in the case of pressed samples, printed and sintered samples were characterized by both geometrical and Archimedes' densities.

Finally, microstructures of sintered bodies were characterized by means of Field Emission Scanning Electron Microscopy observations (FESEM, Hitachi S4000 and Zeiss Sigma 300, Oberkochen, Germany) after sample gold sputtering (SPI Module Sputter Coater, West Chester, PA, USA).

### *2.2. Fabrication of MOFs–Functionalized Mullite Substrates*

HKUST-1 impregnation was carried using the two-steps synthesis of seeding and growth developed in our previous work [47], where the complete protocol is detailed. Reactants ($Cu(NO_3)_2 \cdot 3H_2O$ and 1,3,5,-benzenetricarb-oxylic acid) were supplied by Sigma-Aldrich (St. Louis, MI, USA) and used as received. In brief, a first step of the protocol is dedicated to HKUST-1 nucleation: MOFs seeds were obtained from precursors solutions mixed and heated at 120 °C for 6 h in autoclave. Preheated mullite substrates (60 °C) were then poured into HKUST-1 seeds solution until complete evaporation in oven at 95 °C. After 3 cycles, HKUST-1 seeds not completely adherent were removed by ethanol washing and 1 min sonication. In total, nine depositions and three washings were performed. The

second step is dedicated to crystals growth by heating in an autoclave (6 h, 120 °C) the deposited substrates together with a new precursor solution. Finally, after ethanol washing and 5 min sonication, samples were dried overnight at 100 °C.

HKUST-1 deposited amount was evaluated in terms of weight percentage of gain compared to the blank substrates. HKUST-1 crystals morphology and adhesion to the mullite substrates were characterized by means of FESEM observations. To evaluate specific surface area (SSA), pore volume and pore size of the synthetized MOFs, nitrogen adsorption tests at 77 K (TriStar II by Micromeritics, Norcross, GA, USA) were performed. Samples were degassed for 24 h under vacuum at 150 °C [28,34].

## 3. Results and Discussion

### *3.1. Powders Characterization*

The particle size distribution of Mc and Mf powders are depicted in Figure 2, and the relative $D_{10}$, $D_{50}$ and $D_{90}$ values (corresponding to 10%, 50% and 90% of the cumulative volume distribution) are collected in Table 2. The as-received powders show a multimodal distribution (black lines), with $D_{50}$ values corresponding to 12.8 and 6.6 µm for Mc and Mf, respectively. A water ball-milling of 48 h was needed to decrease the size of the bigger particle population: $D_{50}$ values of ~3.8 and 2.4 µm were reached for Mc and Mf, respectively, while the total distribution was barely narrowed. After drying and calcination at 650 °C/1 h (necessary to decompose the magnesium nitrate, as detailed in Section 2.1.1) a certain agglomeration occurred, providing the final particle size distribution characterized by $D_{50}$ of 9.2 µm (for Mc) and 4.4 µm (for Mf). In addition, Mc powder was characterized by a wider granulometric distribution compared to Mf powder, which has a bimodal and narrower granulometric curve. FESEM micrographs show the effect of ball-milling and calcination on particle morphology. For both Mc and Mf powders, the sharp edges of the as-received powders (Figure 2B,F) appeared smoothed and more rounded after ball-milling, and the particle size seemed consistently reduced (Figure 2C,G). Moreover, after calcination, FESEM micrographs exhibit larger, agglomerated particles, in agreement with the size distribution from laser granulometry (Figure 2D,H).

**Table 2.** $D_{10}$, $D_{50}$ and $D_{90}$, values for Mc and Mf mullite powders in the as-received, 48 h ball-milled (48 h BM) and calcined form. Results of calcined powders, used for shaping the mullite substrates, are highlighted in grey.

| Mullite Powders | | $D_{10}$ [µm] | $D_{50}$ [µm] | $D_{90}$ [µm] |
|---|---|---|---|---|
| Mc | As-received | 1.9 | 12.8 | 44.2 |
| | 48 h BM | 0.8 | 3.8 | 21.8 |
| | Calcined | 1.6 | 9.2 | 34.5 |
| Mf | As-received | 1.1 | 6.6 | 27.2 |
| | 48 h BM | 0.8 | 2.4 | 13.1 |
| | Calcined | 1.1 | 4.4 | 21.9 |

Mc and Mf powders were also characterized by XRD analysis, as depicted in Figure 3. Mullite peaks were indexed according to the JCPDS file number 15-0776. The presence of free aluminum oxide ($\alpha$-$Al_2O_3$) in the hexagonal phase was identified by JCPFD file 96-900-7499. By XRD characterization, no relevant differences in between the patterns of the as received, ball-milled and calcined forms were highlighted, neither for Mc, nor for Mf powders. This confirms that the milling process and the thermal treatment had no effects on ceramic powders composition. $Mg(NO_3)_2$ was homogenized during ball-milling and decomposed into MgO (1 wt%) after calcination. It must be noticed that neither $Mg(NO_3)_2$ in the ball-milled mullite powder, nor MgO after calcination could be detected by XRD analysis due to the small amount added.

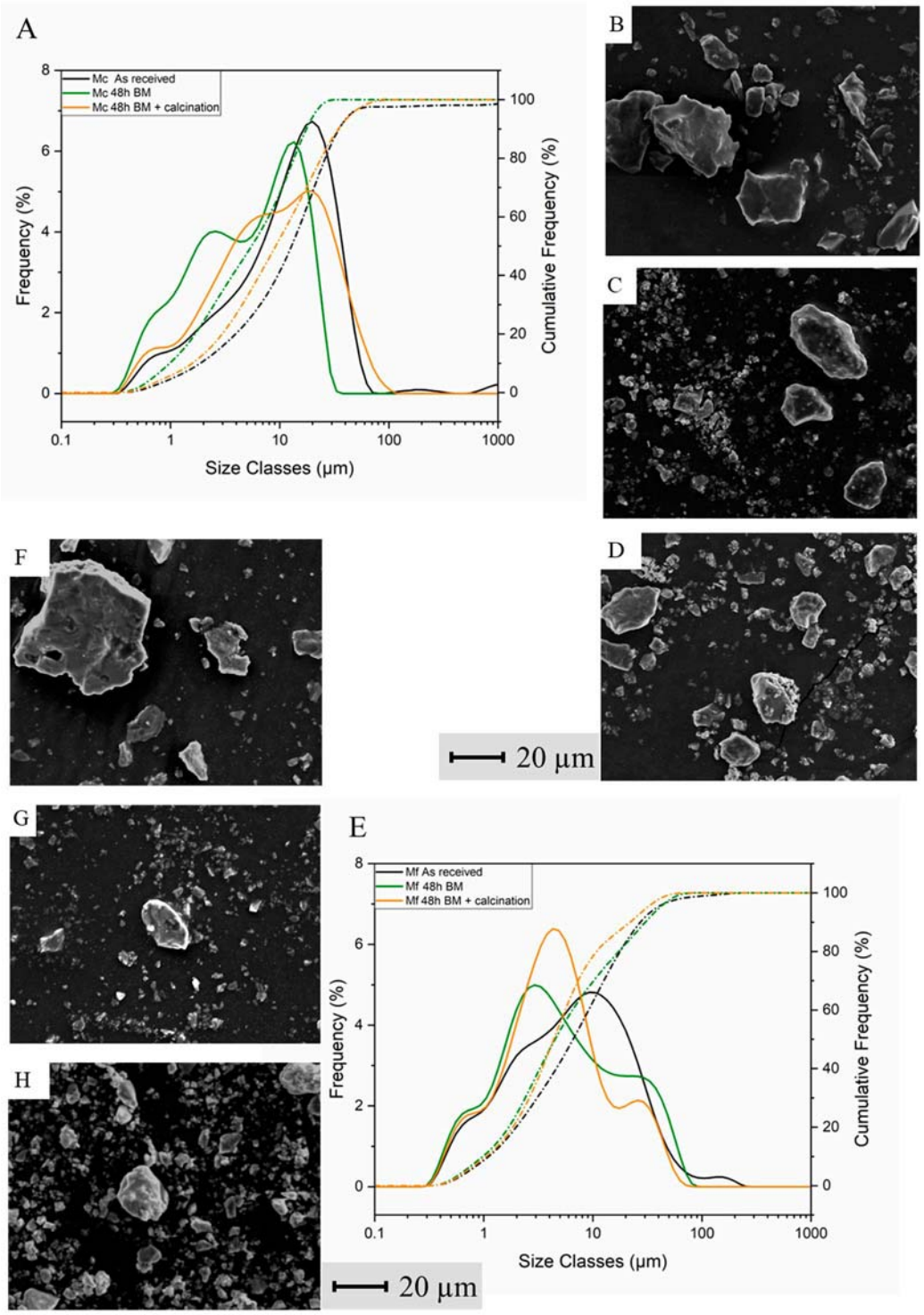


**Figure 2.** Granulometric curves and FESEM micrographs of Mc and Mf (**A**,**E**) powders: characterizations of as-received (black lines, images (**B**,**F**)), ball-milled (BM, green lines, images (**C**,**G**)) and calcined powders (BM + calcination, orange lines, images (**D**,**H**)). Solid and dashed lines represent the relative and cumulative frequency, respectively.

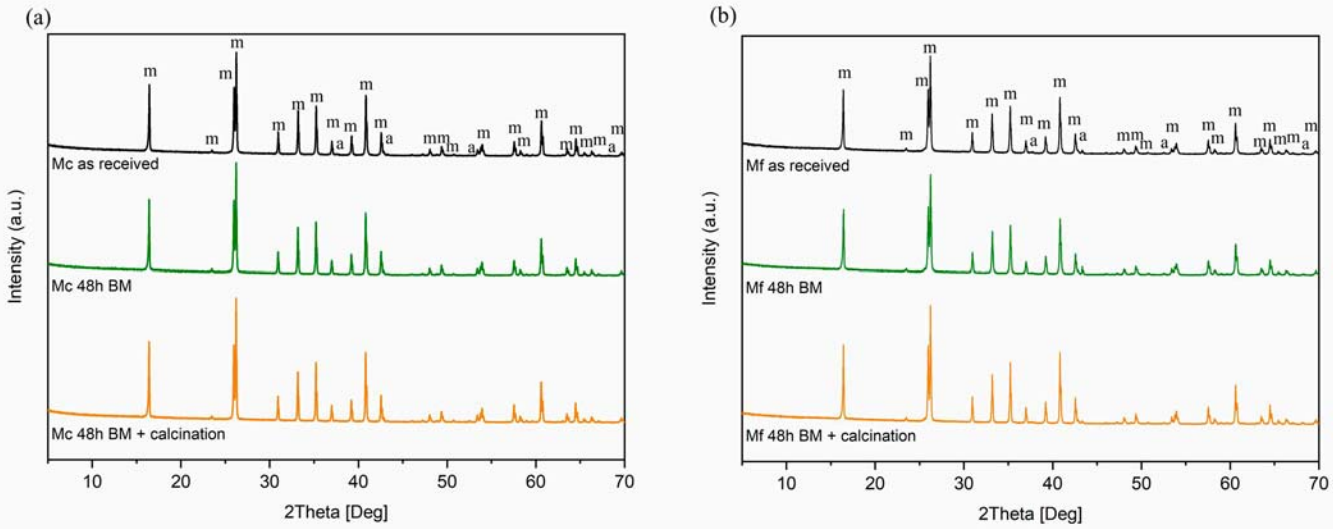


**Figure 3.** XRD patterns of mullite powders: Mc (**a**) and Mf (**b**) in the as-received (black lines), ball-milled (green lines) and calcined (orange lines) form (m = mullite, a = alumina).

XRF analyses (Figure 4) were performed to quantify the impurities and the differences in chemical composition between Mc and Mf, not detectable by XRD. In stoichiometric mullite ($3Al_2O_3 \cdot 2SiO_2$), alumina and silica represent, respectively, 71.8 wt% and 28.2 wt% [72]. Both the powders used in the present work show an excess of aluminum oxide, which was in fact detected as a secondary phase by XRD analysis. In ball-milled and calcined powders, magnesium oxide traces occur, in agreement with the addition of the sintering additive, which was added in the ball-milling step in the water-soluble nitrate form. XRF analysis confirms the presence of the desired MgO amount (1 wt%) after nitrate decomposition [71], for both Mc and Mf mullite after calcination. The presence of other impurities is detected in small amounts. The main compositional difference between Mc and Mf concerns the amount of iron oxide: $Fe_2O_3$ is 0.63 wt% and 0.33 wt% for Mc and Mf, respectively. The doubled amount of iron oxide is probably the explanation for the difference in coloration between the powders (Figure S1), with Mc exhibiting a greyish coloration, turning into a reddish colour after calcination. The addition of up to 0.3% $Fe_2O_3$ and $TiO_2$ in mullite-forming $A1_2O_3$-$SiO_2$ mixtures increases the amount of formed mullite and decreases the content of alumina [73]. For other oxide contents, the difference between Mf and Mc accounts for less than 1 wt%.

### *3.2. Properties of Mullite Slurries for DLP Process*

After mullite powders processing, ball-milled and calcined Mc and Mf mullites were used to prepare ceramic slurries at 42.6 vol% solid loading, (corresponding to 69 wt%) [47]. The addition of 5 wt% dispersant (as respect to the mullite powder) ensured the combination of the advantages of the high solid loading, desirable to guarantee a good densification of DLP printed ceramics, together with a rheological behavior suitable with the shaping process [74,75]. The evolution of the shear viscosity as a function of the shear rate is depicted in Figure 5. At low shear rate, both slurries exhibit shear-thinning properties, before reaching a plateau in the viscosity, where Mf slurries exhibit higher viscosities. Rheological properties are in fact closely related to the particles granulometry. It is generally observed that decreasing particle size and narrowing the granulometric distribution, the slurry viscosity increases [76–79]. In fact, for slurries at the same solid volume, attraction in between ceramic particles is more pronounced when they have smaller sizes and higher surface areas. Nevertheless, both slurries show a very low viscosity (0.4 and 1.3 Pa·s for Mc and Mf containing slurries, respectively) at the operative shear rate of the DLP apparatus, which corresponds to the shear rate applied by the blade during slurry spreading (approx. 160 $s^{-1}$). These values are far away from the maximum values able to ensure the suitable

flowability for the shaping process (3–5 Pa·s, [20,74]); thus, both Mc and Mf showed a rheological behavior compatible with the AM shaping through DLP.

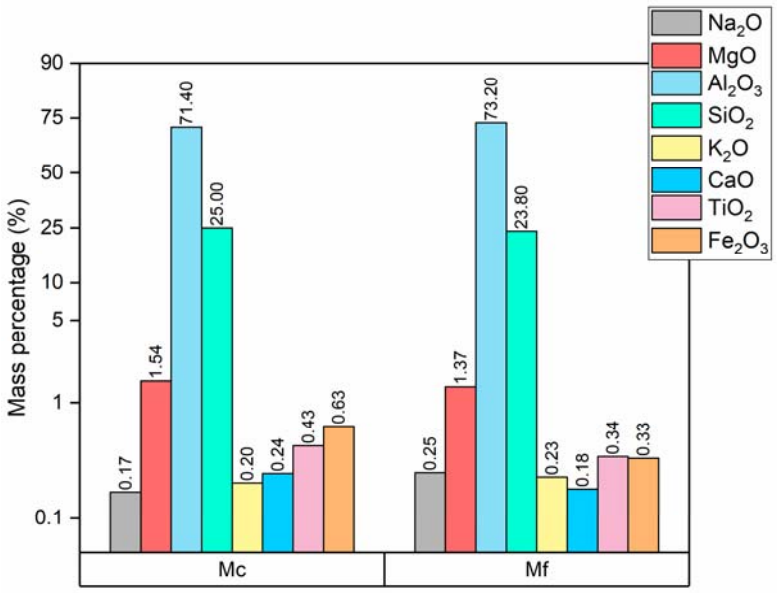


**Figure 4.** XRF analysis: comparison between Mc and Mf.

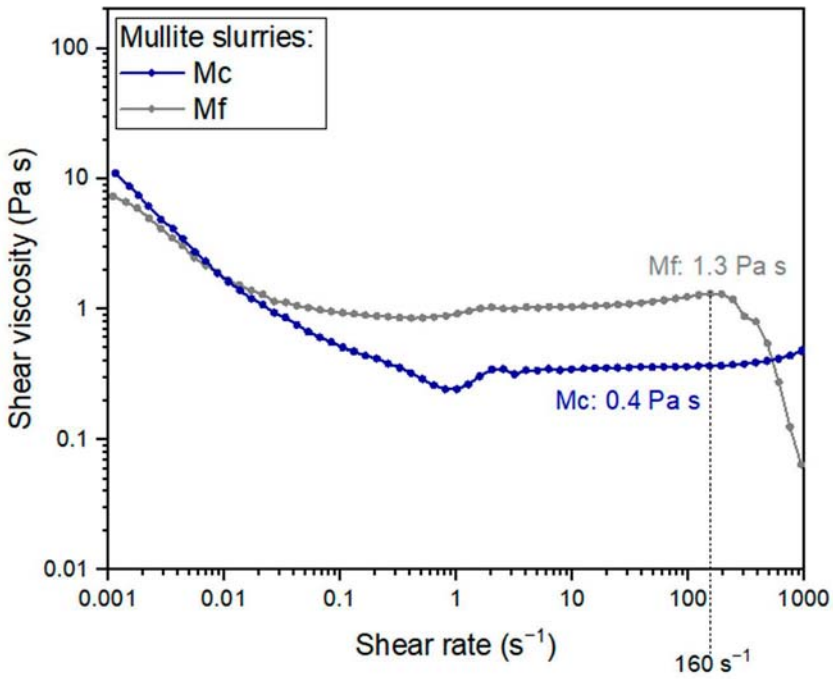


**Figure 5.** Flow curves of mullite slurries prepared with ball-milled and calcined Mc (blue curve) and Mf (grey curve) powders, at 69 wt% solid loading and 5 wt% dispersant.

### *3.3. Pressed and 3D-Printed Pellets: Characterization and Sintering Behavior Evaluation*

Mullite pellets were manufactured using Mc and Mf powders treated as previously explained. Mc and Mf pellets are shown in Figure 6 in the green, as-printed and sintered form. After shaping, samples reflect the difference in coloration observed for the powders (Figure S1): Mc green and as-printed pellets (Figure 6A,E) do not appear perfectly white as the corresponding Mf samples (Figure 6B,F).

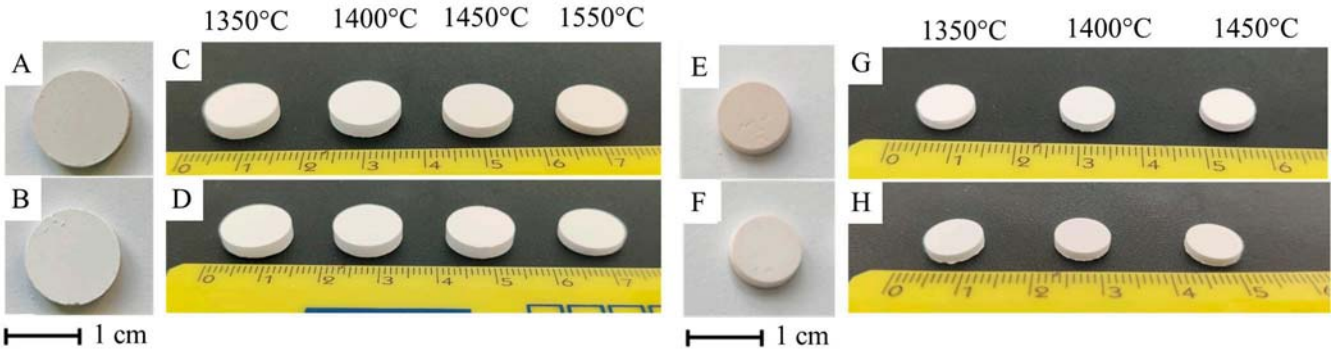


**Figure 6.** Mc (up) and Mf (below) mullite pellets shaped by uniaxial pressing (**A**–**D**) and DLP (**E**–**H**). Samples are shown as green (**A**,**B**), as-printed (**E**,**F**) and after sintering at different temperatures (**C**,**D**,**G**,**H**).

A preliminary evaluation of the sintering behavior of samples shaped by different techniques is crucial to evidence the effect of sintering temperature onto the substrate porosity, with the goal of enhancing the MOFs' adhesion. Dilatometric curves up to 1550 °C of Mc and Mf samples, both printed (green curves) and pressed (black curves) are, respectively, shown in Figure 7a,b. None of the samples achieved 100% of the theoretical density, meaning that the selected maximum temperature (i.e., 1550 °C) is not sufficient to obtain fully dense samples without any dwelling time. Nevertheless, the aim of this study was not to achieve fully dense samples but porous substrates.

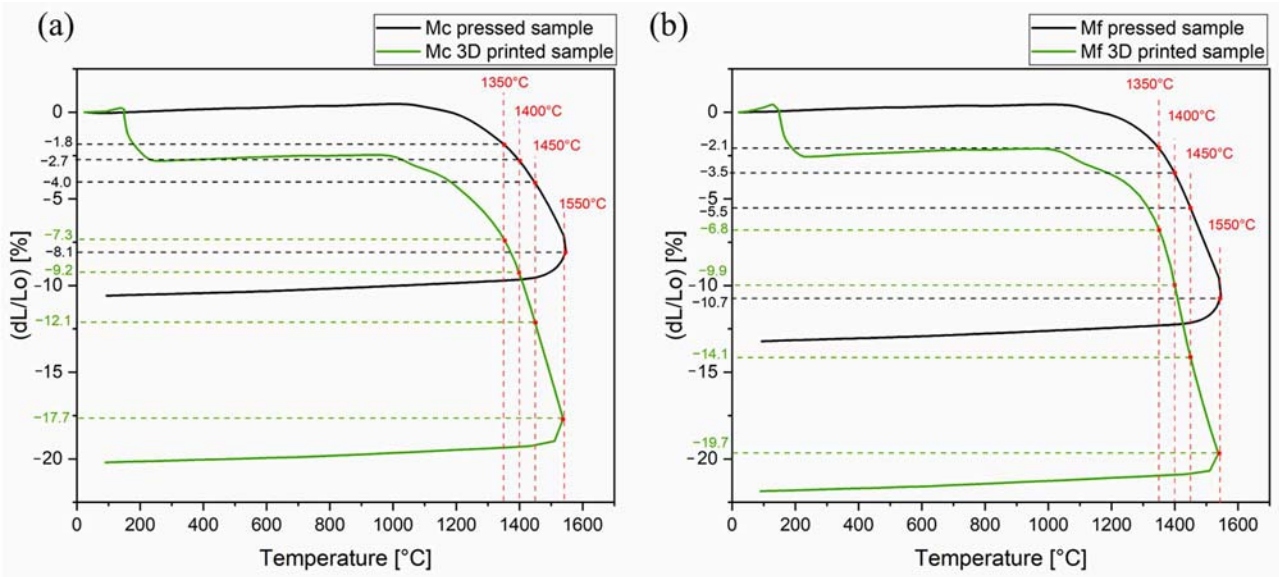


**Figure 7.** Dilatometric curves of Mc (**a**) and Mf (**b**) pressed (black curves) and 3D-printed (green curves) samples. In evidence the points referred to selected sintering.

Table 3 resumes the shrinkage values at 1350 °C, 1400 °C, 1450 °C and 1550 °C for all the samples: these temperatures are highlighted since they were then selected as sintering temperatures. At 1550 °C, pressed Mc and Mf reached a $dL/L_0$ = 8.1 and 10.6%, respectively, corresponding to an undesired high geometrical density of 74.2 and 80.7% (as showed in Figure 7). Thus, for 3D-printed bars, the study focused on $T_{sint}$ below 1450 °C. For both Mc and Mf, 3D-printed samples display higher shrinkage values compared to pressed bars: this is due to the use of a photopolymerizing resin in the additive technique which act as a temporary binder between ceramic particles in the shaping process; it is then responsible of a significant shrinkage when it is burned out before sintering [59,60]. On the other side, the absence of binders in green pressed samples limits the dimensional contraction during the

thermal treatment. Independently of the shaping process and of the sintering temperature, Mc has a lower shrinkage compared to Mf, except for pressed samples at 1350 °C: this could be due to Mc coarser particle size in comparison to the thinner Mf one.

**Table 3.** Shrinkage at different temperatures (1350, 1400, 1450 and 1550 °C) from dilatometric analyses of Mc and Mf samples formed by uniaxial pressing and DLP.

| | Tsint (°C) | Pressed Samples $dL/L_0$ (%) | 3D-Printed Samples $dL/L_0$ (%) |
|---|---|---|---|
| Mc | 1350 | −1.8 | −7.3 |
| | 1400 | −2.7 | −9.2 |
| | 1450 | −4.0 | −12.1 |
| | 1550 | −8.1 | −17.7 |
| Mf | 1350 | −2.1 | −6.8 |
| | 1400 | −3.5 | −9.9 |
| | 1450 | −5.5 | −14.1 |
| | 1550 | −10.7 | −19.7 |

DLP printed and pressed pellets sintered at different temperatures are compared in terms of geometrical and Archimedes' density (Figure 8a,b) and directional shrinkages values (Figure 8c,d). Even though the differences in density values between samples sintered at different temperatures are not that significant, an expected increase in both geometrical and Archimedes' densities can be noted with the sintering temperature. In addition, the significant difference between the two densities values suggests the relevant presence of an open porosity that is beneficial for the final aim of this study. Sintering behavior and porosity values, as well as geometrical and Archimedes' densities measured with different techniques are in agreement with literature data [55,70]. In particular, it is reported that mullite membranes sintered at 1300 °C show a porosity between from 42% to 58%, while it reaches 47.21 to 64% when sintered at 1400 °C [55,70]: specifically with 1 wt% of additive and sintering at 1550 °C without dwelling time final densities of ca. 60% and ca. 70% of the theoretical value were achieved.

Graphs in Figure 8 clearly underline the differences between DLP shaped and pressed samples, in particular the easier densification of the latter ones. In fact, geometrical density values for the same sintering temperature are always higher for pressed samples compared to 3D-printed pellets. For the same sintering temperature, DLP samples show 9–10% higher total porosity and 5% higher open porosity when compared to the correspondent pressed pellets. The intrinsic differences between shaping procedures are underlined also by the gap between geometrical density of as-shaped and green samples. While for ceramic uniaxial pressing, a binder is not mandatory, it is well known that ceramic additive manufacturing by DLP implies the production of as-printed samples made up of ceramic particles bonded by the photopolymerized resin, which is then burned out before sintering [59,60]. Hence, the resin can act as a porogen agent to induce further porosity to the material; thus, despite optimizations of solid loading and thermal treatments, DLP shaped samples show a lower density with respect to pressed samples.

Shrinkage data are displayed in Figure 8c,d and are consistent with considerations about densification trends: in particular, volumetric shrinkage is higher for 3D-printed pellets than for pressed pellets, and in both cases shrinkage increases with the sintering temperature. Concerning the z and x-y plane contraction, their gap is inverted. This is because the shaping process has effects on the shrinking behavior: for 3D-printed pellets, contraction among the printing direction is expected to be higher than in the x-y plane to guarantee a good layer adhesion. On the other hand, in almost all uniaxially pressed pellets, the z contraction is lower than on the x-y plane since it corresponds to the pressing direction.

Finally, comparing the different mullites, Mc pellets show in general higher densities and lower shrinkage. Mc has higher sintering capability and densification, even if the MgO sintering additive amount is the same in the two mullite powders. However, Mc has a higher iron oxide content and a different particle size distribution than Mf, which could

explain this result [73]. Thus, the data displayed here are in accordance with dilatometric analyses (Figure 7) and confirm that Mc is characterized by a greater tendency to densify compared to Mf.

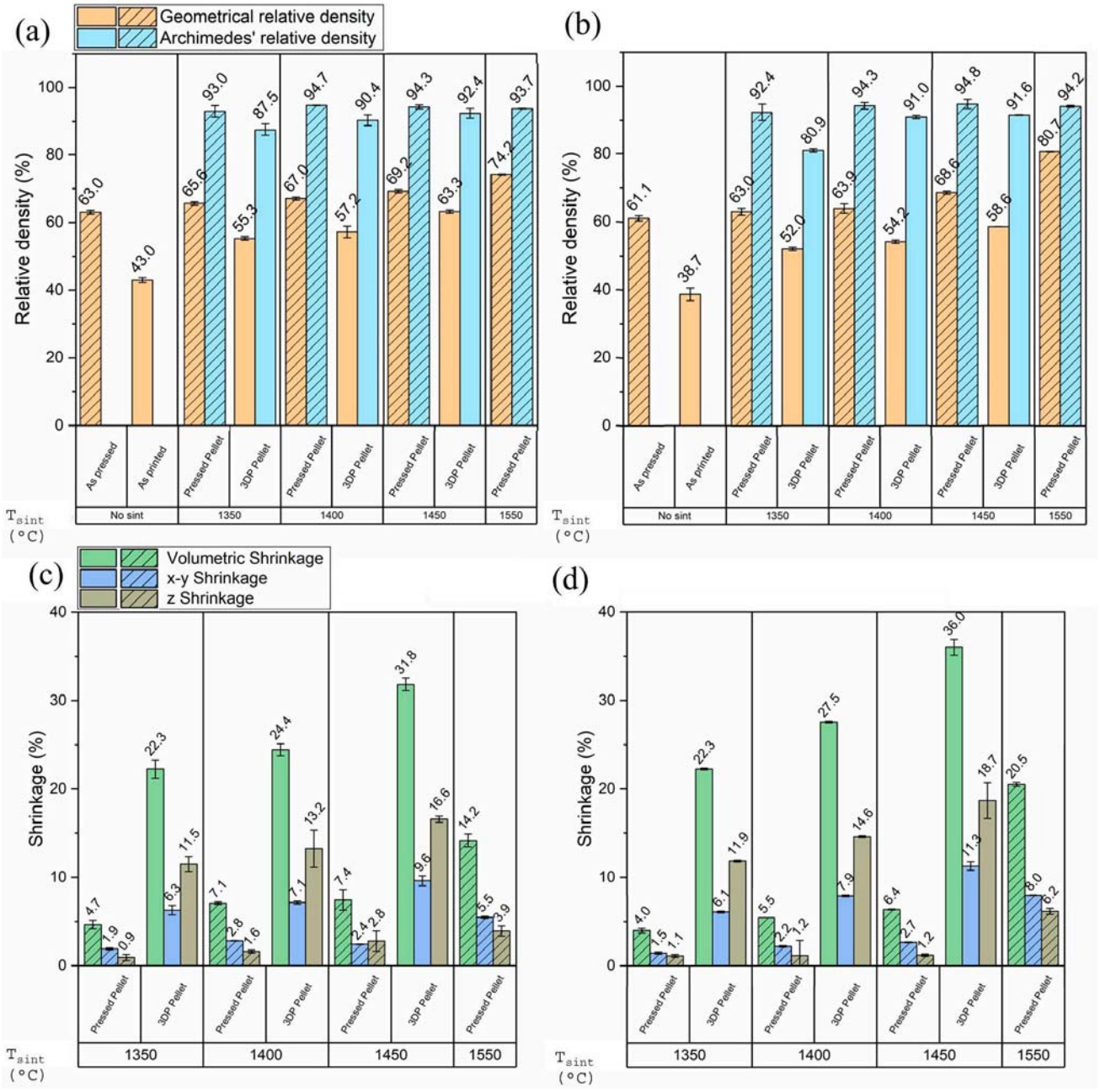


**Figure 8.** Properties of pressed and 3D-printed mullite samples, realized with Mf (**left**) and Mc (**right**) mullite and sintered at different temperatures: geometrical and Archimedes' relative densities (**a**,**b**); volumetric, x-y and z shrinkage (**c**,**d**). The error bars are calculated as difference between the highest and lowest values; this is measured on a minimum of 2 samples and a maximum of 4.

The influence of the sintering temperature on the porosity of the mullite pressed pellets was also studied by Mercury Intrusion Porosimetry (MIP), as displayed in Figure 9. The percentage of porosity decreases by increasing the sintering temperature, as does the total pore area. On the other hand, since only the largest open porosities are not totally occluded, the average diameter of the remaining open porosities increases. These results therefore demonstrate that a higher sintering temperature promotes densification, reducing the total

pore area and increasing the average pore size. The comments are consistent with what is shown by the graphs of incremental mercury intrusion in Figure S2**.** Comparing the two mullite powders, Mf samples exhibit a higher open porosity percentage compared to Mc ones when sintering is carried at 1350 °C, 1400 °C and 1450 °C. Thus, Mc at lower temperatures has a smaller pore volume than Mf, but a larger pore size: this is probably due to the coarser grain size of Mc. Mf, on the other hand, has a smaller pore size, since it is a finer powder, but a larger volume: this is because Mf has less iron oxide and therefore densifies less than Mc, consistent with what was observed previously. At the highest temperature studied (1550 °C), the pore area values are almost equal but the difference in pore size remains.

Table 4 compares open porosity values measured by MIP for both Mc and Mf pressed pellets, with open porosity ($P_g$) calculated from the total porosity (obtained from the geometrical density) subtracting the close porosity estimated by Archimedes' measurements. The values are comparable and show the same trend; however, $P_g$ is always found smaller, probably due to an overestimation of the close porosity by Archimedes' method. As expected, open porosity increases by lowering the sintering temperature.

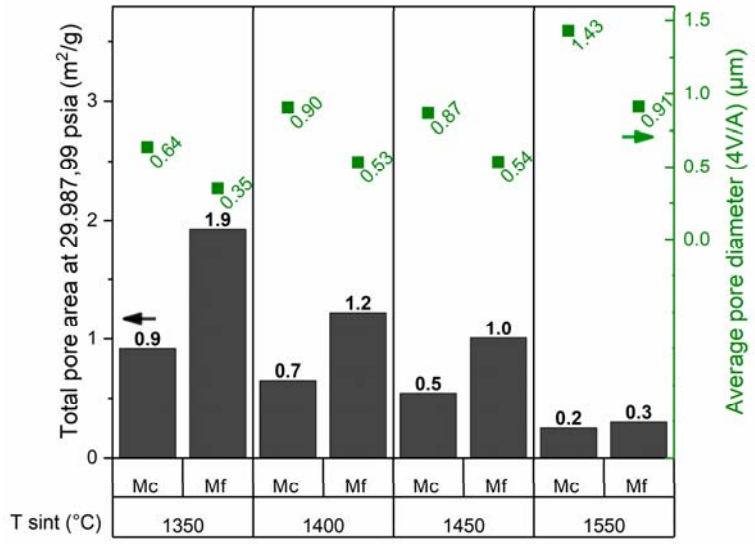


**Figure 9.** Total pore area and average pore diameter determined by MIP of Mc and Mc pressed pellets sintered at 1350 °C, 1400 °C, 1450 °C and 1550 °C.

**Table 4.** Porosity of Mc and Mf pressed pellets sintered at 1350 °C, 1400 °C, 1450 °C and 1550 °C measured via MIP and open porosity ($P_g$).

| | Tsint (°C) | Open Porosity (MIP) (%) | Open Porosity (Pg) (%) |
|---|---|---|---|
| Mc | 1350 | 33.5 | 25.3 |
| | 1400 | 33.6 | 27.7 |
| | 1450 | 29.1 | 24.8 |
| | 1550 | 23.4 | 19.5 |
| Mf | 1350 | 37.0 | 27.4 |
| | 1400 | 36.2 | 30.4 |
| | 1450 | 32.0 | 26.2 |
| | 1550 | 19.0 | 13.5 |

Mullite microstructures were then investigated by FESEM observations in order to highlight the effect of shaping process, sintering temperature and mullite type. Pressed samples' fracture surfaces were observed without polishing and results are shown in Figure 10. The microstructure is mainly homogeneous since the pressing process does not lead to

significant differences in the spatial axes. For both Mc and Mf pressed pellets, densification is more evident at higher sintering temperature, conferring to the sintered specimens a quite good handling, but the microstructure still shows a low coalescence between ceramic particles. In particular, after sintering at 1350 °C (Figure 10A,E), and 1400 °C (Figure 10B,F), FESEM micrographs still display well-defined and not aggregated ceramic particles (red circles in the figure). As expected, increasing the sintering temperature solid state diffusion is promoted and consequently grain coalescence (green arrow), clearly evident for 1550 °C heat-treated samples (Figure 10D,H). Nevertheless, since interparticle porosities (blue arrow) are still present even at the highest sintering temperature investigated here, the full densification is not reached, in agreement with density measurements (Figure 8). SEM micrographs of 3D-printed samples are displayed in Figure 11, obtained after polishing to better highlight the microstructure resulting from the additive manufacturing shaping. In particular for Mf samples, printing layers are clearly evident and their thickness (between 20 and 30 μm, as indicated by the red arrows in the pictures) is comparable with the nominal layer thickness (30 μm). The same considerations as for the pressed samples can be made when comparing different sintering temperatures. Furthermore, as expected from measured densities and porosities previously showed, FESEM micrographs also highlight the higher open porosity occurrence for 3D-printed samples compared to uniaxially pressed ones.

### *3.4. Substrate Characterization: Effect of Sintering Temperature on MOFs Functionalization*

HKUST-1 crystals were synthetized by solvothermal synthesis, nucleated, and grown on mullite 3D-printed pellets to confer gas separation and $CO_2$ capturing properties [47]. From the pictures of the functionalized substrates, shown in Figure 12, a visible difference in color intensity due to the presence of HKUST-1 as a function of the sintering temperature can be observed: the coating appears more intense and homogeneous for more porous pellets, especially for Mc samples, confirming the positive effect of porosity on the deposition and adhesion of HKUST-1.

Figure 13 shows the XRD patterns of HKUST-1 crystals synthesized by solvothermal method (blue line). The process led to the formation of pure [$Cu_3(BTC)_2$]. The pattern, in fact, is comparable with literature data, both with computational pattern and experimental studies [80–84]. The synthesized [$Cu_3(BTC)_2$] does not exhibit any peaks corresponding to unreacted copper oxide species, such as $Cu_2O$ ($2\theta$ = 36.43°) or CuO ($2\theta$ = 35.5° and 38.7°) [80,82], indicating the formation of highly pure HKUST-1 compounds, without any unreacted phase. Hence, the XRD evaluations highlight the high purity and correct stoichiometry of HKUST-1 solvothermally synthetized in the current study. XRD analyses on the HKUST-1-coated substrates highlight the successful HKUST-1 growth on the Mc or Mf ceramic supports (respectively, shown in Figure 13a–d) for all the three-sintering temperature: 1450 °C (red), 1400 °C (orange) and 1350 °C (black). HKUST-1 peaks on functionalized ceramic pellets are significantly less intense when compared to the signal of mullite substrate, as expected due to the low amount of HKUST-1 in the sample, and the weak contrast of HKUST-1 (made of light elements, H, C, O) compared to copper sites in mullite: this is expected since, in the case of polycrystalline thin layers, most of the X-ray beam passes through the coating and is scattered by the substrate [85]. In fact, the X-ray CuK$\alpha$ radiation ($\lambda$ = 0.154056 nm) has a penetration depth of ca. 20 μm [86], so higher than the HKUST-1 layer thickness (about ten μm as displayed in Figure 14). In addition, HKUST-1 crystals are mostly made of light elements (H, C, O), except for the copper atoms, and they are easily crossed by X-rays. However, despite their low intensity, the insights in Figure 13c,d clearly highlight the presence of peaks at 2-theta angles in the range 5–14°, which is unequivocally attributed to HKUST-1 [47,65] and can be distinguished from mullite characteristic reflections occurring at higher angles. A slight horizontal peak shift can be noticed, probably due to the different specimen geometry (MOFs powders vs. MOFs coated mullite pellets), sample positioning and surface charge fluctuation [87]. In addition, comparing Mc and Mf, for the three investigated temperatures, MOFs signals are

more intense for Mf than Mc samples which could be related to the lower densification and higher porosity of those samples. Thus, $Cu_3(BTC)_2$ was successfully synthetized by seeding the support with micrometric crystals and the MOFs signals intensity can be related to ceramic support porosity.

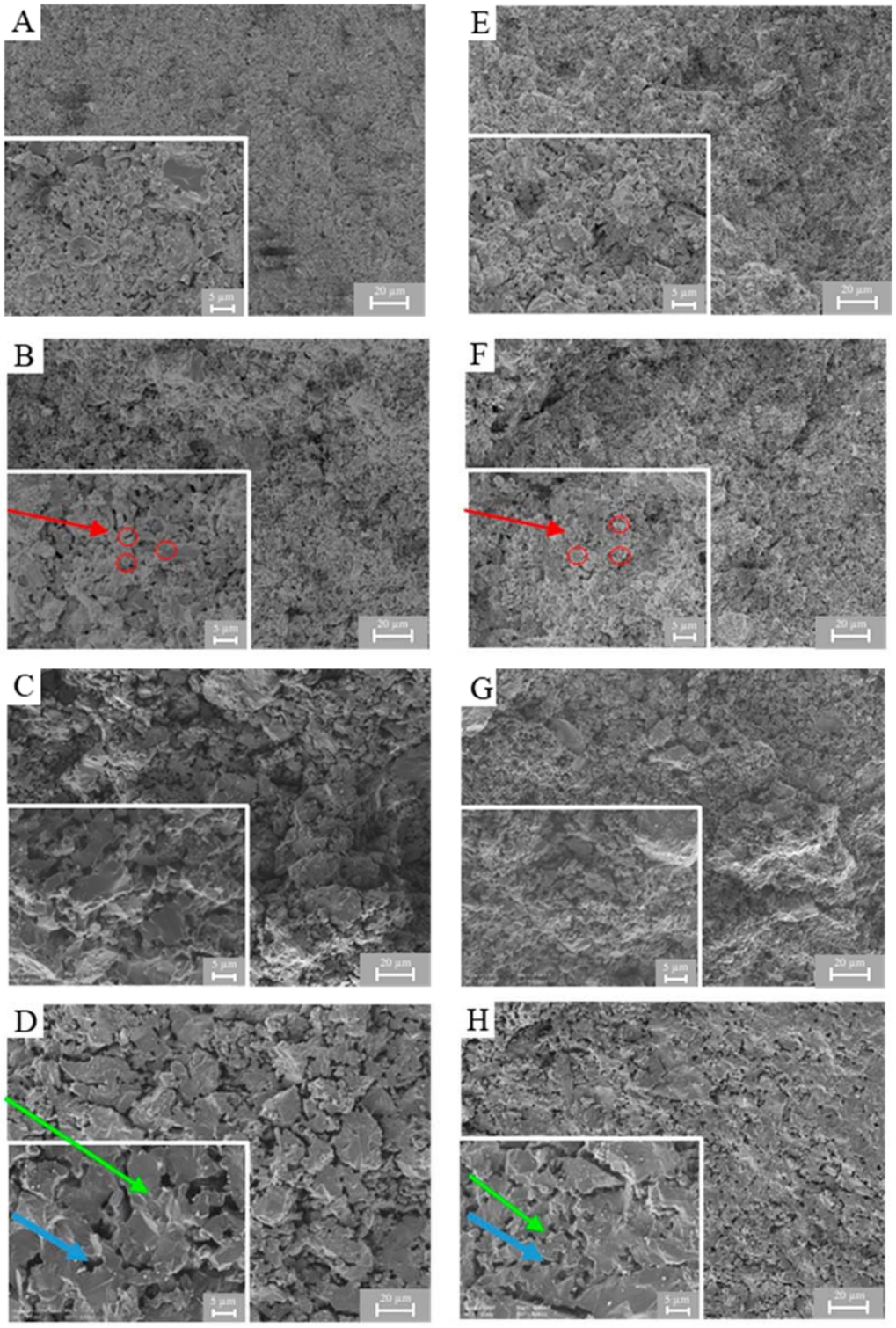


**Figure 10.** FESEM micrographs of pressed pellets: microstructures of Mc (**left**) and Mf (**right**) samples sintered at 1350 °C (**A**,**E**), 1400 °C (**B**,**F**), 1450 °C (**C**,**G**) and 1550 °C (**D**,**H**). Signs of non-coalescence are underlined in red, coalesce in green and uncomplete densification in blue.

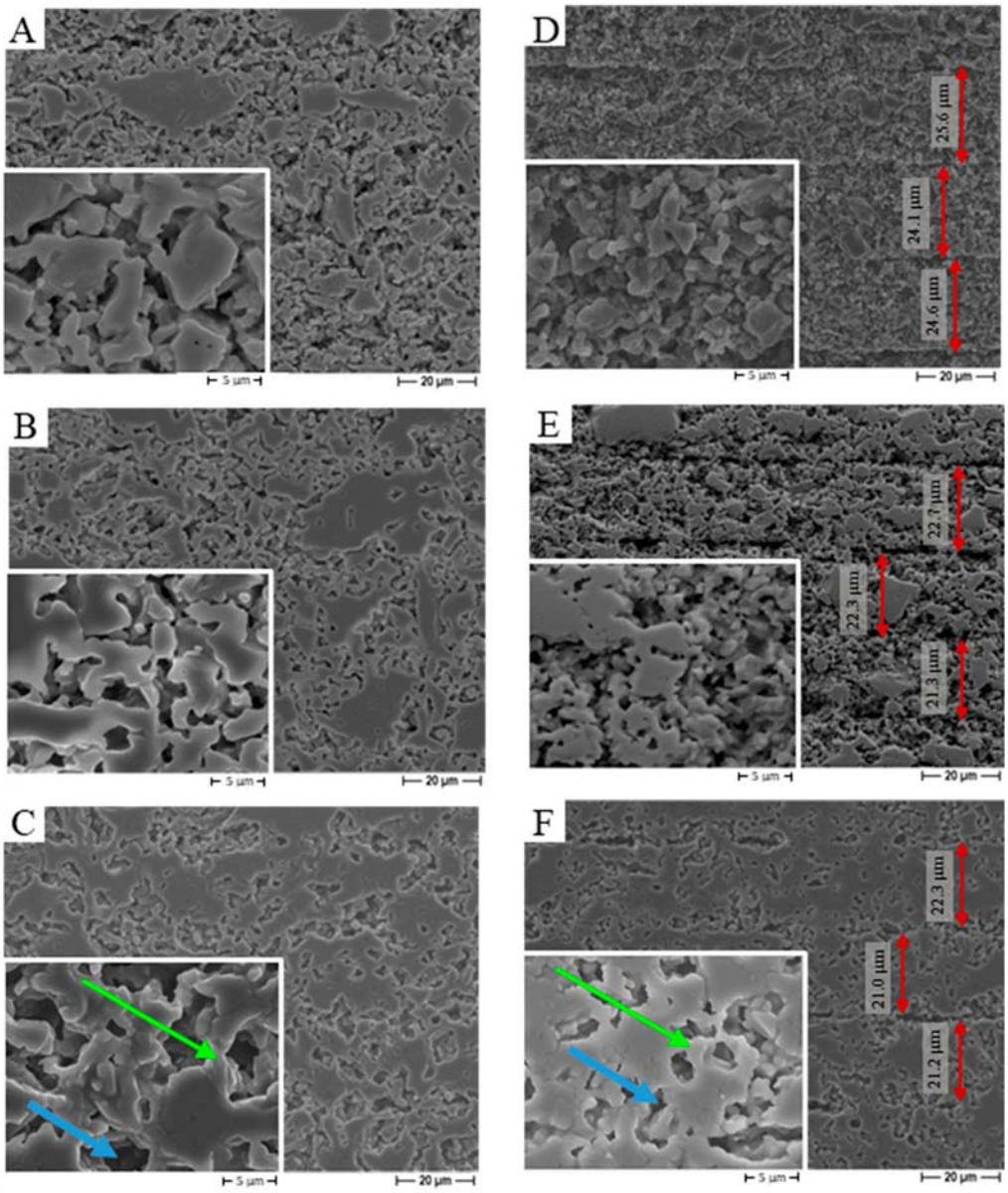


**Figure 11.** FESEM micrographs of 3D-printed pellets: microstructures of Mc (**left**) and Mf (**right**) samples sintered at 1350 °C (**A**,**D**), 1400 °C (**B**,**E**) and 1450 °C (**C**,**F**). Signs of coalescence are underlined in green and uncomplete densification in blue.

HKUST-1 crystals' adhesion on mullite substrates was confirmed through FESEM observations for samples realized by pressing and 3D printing technique, respectively, shown in Figures S3 and 14. An effective formation of a thin coating film was successful for all samples, since all the micrographs confirmed the presence of a MOFs crystalline layer on mullite microstructure. The crucial effect of lowering the sintering temperature and increasing porosity is highlighted also by microscopy evaluations: as is evident observing Figure 14B, MOFs structures (green arrows) are embedded into the substrate open porosity. If comparing it with Figure 14F, this phenomenon is deterred in substrates sintered at higher temperature, where instead a sharp boundary between MOFs and mullite is displayed. Furthermore, observing Figure 14A,G especially in comparison with Figure 14D,N, the cuboctahedral morphology typical for HKUST-1 grown crystals, can be noticed and it seems better developed on substrates sintered at lower temperatures. Furthermore, 3D-printed substrates seem to promote both MOFs adhesion and morphological development more efficiently when compared to pressed and less porous pellets (Figure S3).

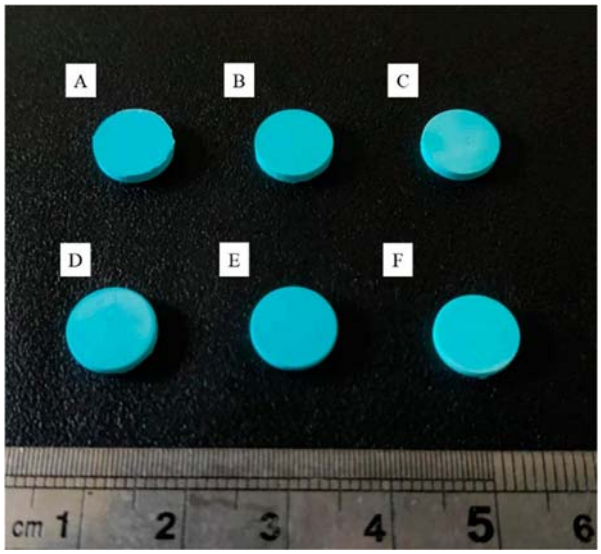


**Figure 12.** HKUST-1 coating on 3D-printed Mc (**up**) and Mf (**down**) mullite pellets, sintered at different temperatures: 1350 °C (**A**,**D**), 1400 °C (**B**,**E**), 1450 °C (**C**,**F**).

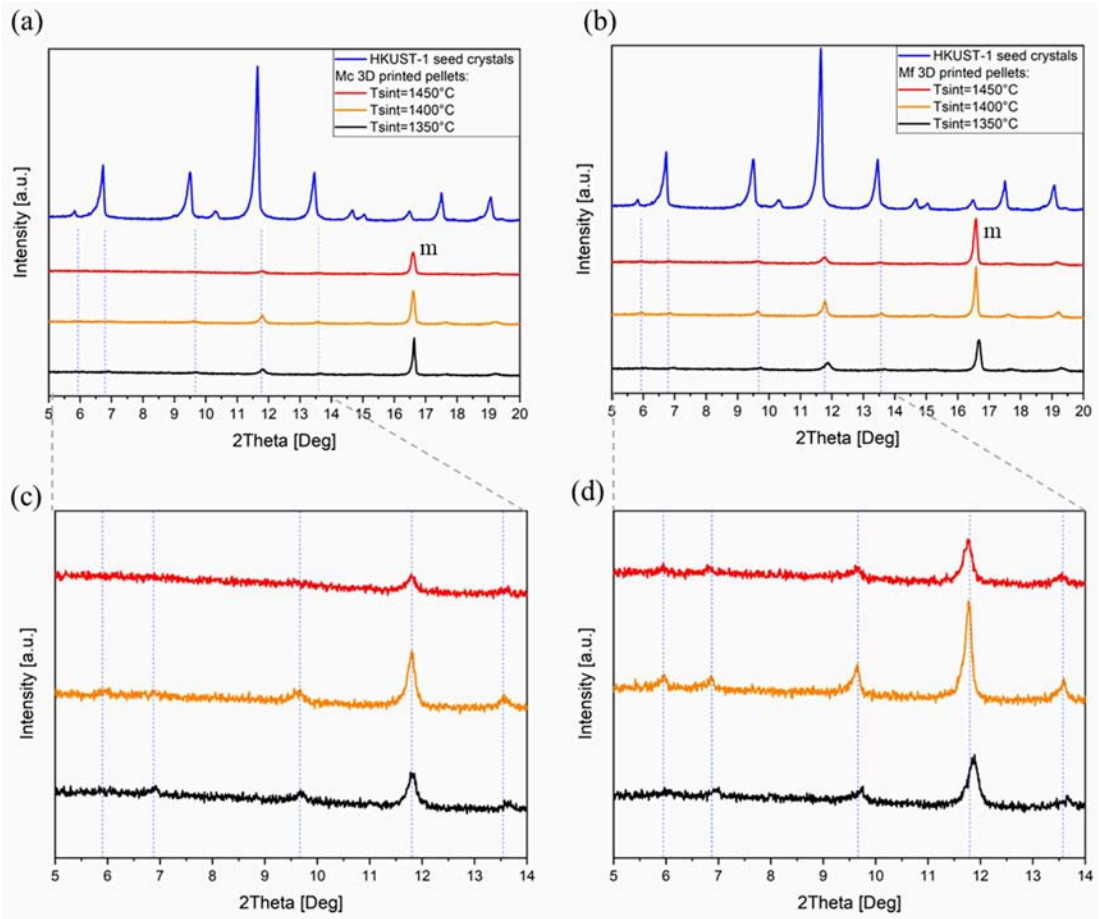


**Figure 13.** XRD patterns of synthesized HKUST-1 (blue line) on Mc (**a**,**c**) and Mf (**b**,**d**) mullite 3D-printed substrates sintered at 1450 °C (red lines), 1400 °C (orange lines) and 1350 °C (black lines); (m = mullite).

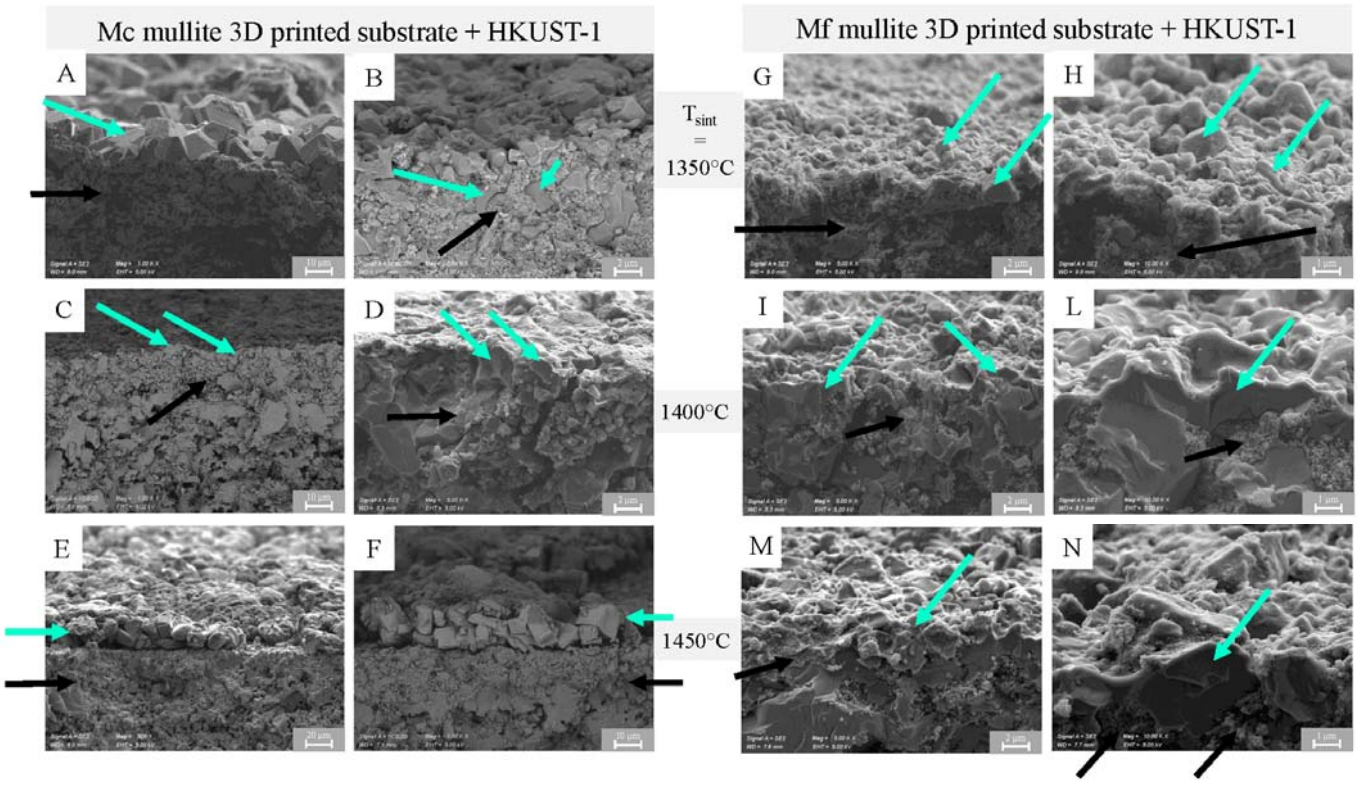


**Figure 14.** FESEM micrographs of HKUST-1 crystals (green arrows) on mullite 3D-printed substrates (black arrows, Mc on the **left** and Mf on the **right**). Samples sintered at 1350 °C (**A**,**B**,**G**,**H**), 1400 °C (**C**,**D**,**I**,**L**) and 1450 °C (**E**,**F**,**M**,**N**).

The mass quantification of MOFs grown onto the ceramic substrates (Figure 15) was crucial to quantitatively evaluate the functionalization efficiency. HKUST-1 gain was measured in terms of weight percentage compared to the blank mullite samples weight, and it is correlated with the total porosity obtained from the relative geometrical density, previously displayed in Figure 8.

Sintering temperature increase led to the same effect for all the investigated samples: the higher the sintering temperature, the higher the substrate density, leading to a lower HKUST-1 amount grown onto the mullite surface. Thus, the porosity of the substrate enhances MOFs seeds fixing. On the one hand, this could be due to the pores, able to better entrap crystals than a smooth flat surface. On the other hand, the rough and porous surface is able to enhance the interactions between the hydroxyl groups on the ceramic surface and the free carboxylic groups belonging to the $Cu_3(BTC)_2$ structure [65], promoting in this way the coating adhesion and continuity. For the same sintering temperature, pressed pellets reached higher densification than 3D-printed pellets, as explained before. Coherently, at the same sintering temperature (i.e., 1450 °C), 3D-printed substrates are better functionalized than the respective pressed samples: thus, the extra porosity introduced by DLP enhances the functionalization. The best results are provided by Mf 3D-printed pellets, which, after sintering at the lowest temperature (1350 °C, geometrical density 52%), show the highest porosity and HKUST-1 uptake (3.5 wt%). Mf samples reached for all the three investigated temperatures the lower geometrical density, leading to higher HKUST-1 superficially grown, except for the highest sintering temperature. In fact, at $T_{sinter}$ = 1450 °C, Mc slightly overcomes the respective Mf pellets in terms of HKUST-1 solid loading (2.3 > 1.8 wt%), even if the density is higher (63.3% respect to 58.6%). Gaps are not dramatic but still relevant and can be due to the compositional difference between Mc and Mf, in other words the iron oxide amount, that is twice in Mc powders. Although Mc is more prone to densification, it seems more convenient when rising the sintering temperature up to 1450 °C, since a higher MOFs amount in comparison to the respective Mf sample can be reached. Thus, it is

because iron oxide plays a dual role: on one hand, it acts as a sintering additive causing the lower porosity of Mc substrates, as observed in the previous section. On the other hand, iron oxide may also provide advantages for MOFs adhesion on mullite thanks to the interaction between MOFs and the $Fe_2O_3$ present on the ceramic surface: in fact, the affinity between the copper centers in HKUST-1 and Fe ions was already reported in literature for other systems [88–90]). Since the iron oxide amount is relatively low (0.66 and 0.33 wt% for Mc and Mf, respectively), this second aspect shows its positive effect and provides actual improvements only at the higher sintering temperature, when the most prominent role of substrate porosity is limited by the higher densification.

Additionally, the main aspect affecting HKUST-1 adhesion is given by porosity, which can be opportunely tuned by controlling the sintering temperature.

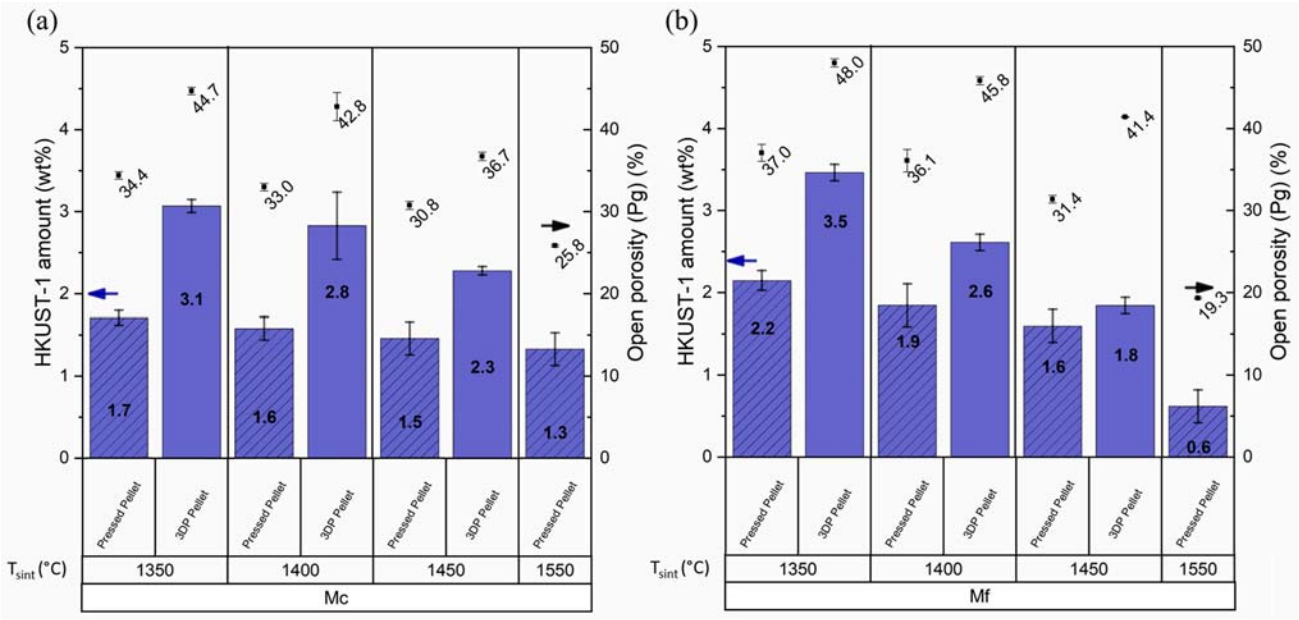


**Figure 15.** HKUST-1 depositions on mullite pellets: MOFs wt% (blue bars) and open porosity (black points) of samples sintered at different temperatures and shaped by DLP or uniaxial pressing. Mc (**a**) and Mf (**b**) mullite were used. The error bars are calculated as difference between the highest and lowest values; it is measured on a minimum of 2 samples and a maximum of 4.

This work represents an in-depth study of the differences between two shaping technologies and two different mullites, investigating Mc and Mf behavior and optimizing their use to produce geometrically complex architectures functionalized with HKUST-1 for CCS. The next steps are to study in detail the $CO_2$ adsorption capacity of this CCS system. In particular, the attention will be focused on Triply Periodic Minimal Surfaces (TPMS) such us Schwartz Primitive or gyroid. As already demonstrated with a different mullite powder [47], such designs could provide higher specific surface area and thus offer several advantages such as improvements in HKUST-1 deposition amount and contact time with $CO_2$. The optimal sintering temperature will need to balance the desired microstructural porosity together with the structural resistance and handling of the final monoliths. Despite the advantages obtained by sintering at 1350 °C observed in the current work, for more complex architectures, such a low temperature is not high enough to ensure a correct sintering and handling of the substrates (Figure 16). Indeed, to avoid dramatic structural damage, a sintering temperature of 1450 °C has to be set for geometrically complex monoliths.

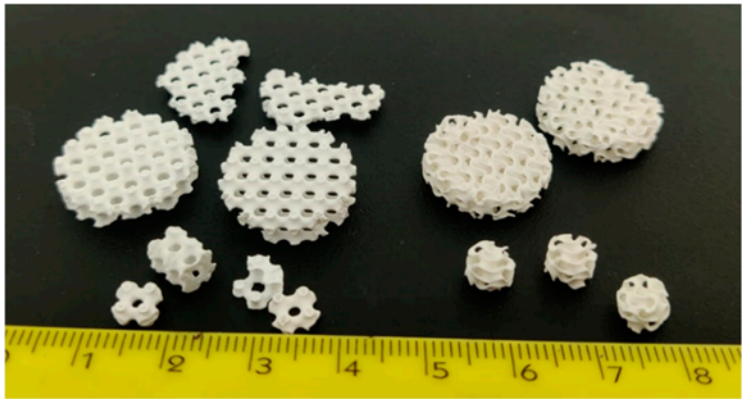

**Figure 16.** Structural damage of geometrically complex mullite architectures shaped by DLP and sintered at temperatures lower than 1450 °C.

Thus, the aim of the current work is not to provide a unique sintering temperature recommended for any type of supports, but to give guidelines and explanations about the interaction between MOFs and mullite supports with difference in porosity and microstructure. The study here reported was essential for the development and MOFs functionalization of complex TPMS mullite architectures using Mc and Mf mullites (Figure 17). Complex mullites architectures were crucial to increase the HKUST-1 deposited on the ceramic surface: TPMS monoliths sintered at 1450 °C reached up to 4 wt% of HKUST-1, almost doubling the MOFs amount adherent on 3D-printed pellets for the same sintering temperature.

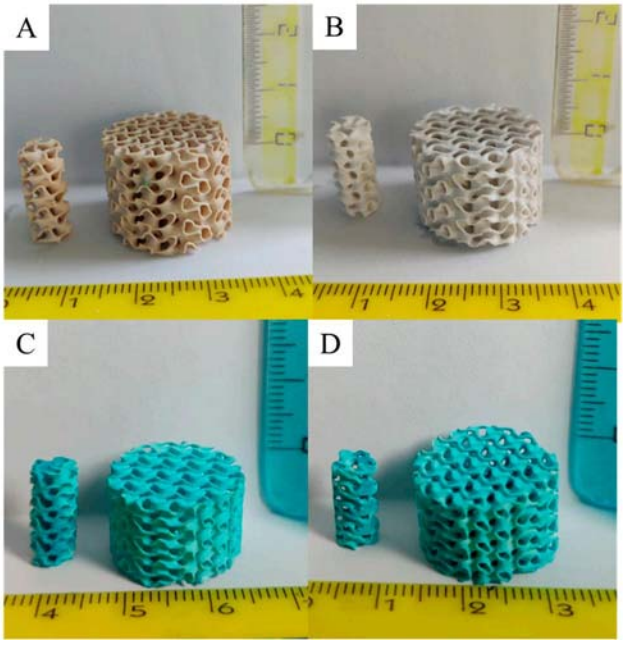


**Figure 17.** TPMS gyroid monoliths shaped by DLP (**A**,**B**) using Mc (**left**) and Mf (**right**) mullite, sintered at 1450 °C and coated with HKUST-1 (2–4 wt%) (**C**,**D**).

## 4. Conclusions

In this work, CCS ceramic supports were produced using two mullite powders (Mc and Mf) differing in particle size distribution and iron oxide content. Functionalization with a microporous coating of HKUST-1 was studied and promoted by $Fe_2O_3$ impurities and substrate porosity.

Mullite powders were carefully characterized (laser granulometry, FESEM observations, XRD and XRF analyses) in as-received, ball-milled and calcined forms. Ball-milled and calcined Mc and Mf powders were used to shape pellets with two forming methods: traditional uniaxial-pressing and additive manufacturing by DLP technology. For this latter process, ceramic slurries were realized mixing a photosensitive commercial resin with mullite powders (solid loading of 69 wt%): both Mc and Mf formulations displayed a shear viscosity compatible with DLP (respectively, 1.3 and 0.4 Pa·s at 160 $s^{-1}$). Mc and Mf samples pressed or shaped by DLP were sintered at three different temperatures (1350 °C, 1400 °C and 1450 °C). Mc 3D-printed pellets reached a geometrical density of 55.3%, 57.2% and 63.3% and Archimedes' density of 87.5%, 90.4% and 92.4%, respectively, setting 1350 °C, 1400 °C and 1450 °C as sintering temperatures. Mf 3D-printed samples showed both lower geometrical (52%, 54.2%, 58.6%) and Archimedes' densities (80.9%, 91.0% and 91.6%) after sintering at the same temperatures. As expected, the higher the sintering temperature, the higher the density achieved. Comparing the two powders, Mf 3D-printed samples display a lower densification degree compared to Mc ones. At the same sintering temperature Mf samples maintain higher porosity compared to Mc, despite Mf finer particle size which should enhance particle coalescence during sintering. This could be due to the compositional differences between the two powders and in particular to iron oxide content: the weight percent of iron oxide amount is two times higher in Mc in respect to Mf (0.63 wt% versus 0.33 wt%), and it acts as a sintering additive promoting densification.

An MOF coating was deposited on mullite samples to confer CCS properties. XRD patterns confirmed that HKUST-1 was successfully synthetized by seeding the support with micrometric crystals and the signals of the coating are more intense for more porous samples, sintered at lower temperature. Mf mullite leads to better results in terms of MOFs coating, coherently with what showed before in terms of lower densification. The HKUST-1 wt% uptake for Mc and Mf 3D-printed supports were, respectively, 3.3%, 2.4%, 2.1% and 3.5%, 2.6% and 1.8%, after sintering at 1350 °C, 1400 °C and 1450 °C. Thus, this work demonstrated how it is possible to enhance the functionalization efficiency accurately tuning the thermal treatment, specifically lowering the sintering temperature and properly choosing mullite powder. The positive effect of the porosity of the ceramic substrate could be determined by the combination of two phenomena. On one hand, higher porosity increases the surface available for MOF adhesion. On the other hand, the rough and porous surface can enhance the interactions between the hydroxyl groups on the ceramic surface and the free carboxylic groups belonging to the $Cu_3(BTC)_2$ structure [65], promoting in this way the coating adhesion and continuity. In further development of 3D-printed monoliths with complex architectures, the sintering temperature selection will be performed while balancing the need of microstructural porosity and the other aspects highlighted in the current work, together with the structural resistance and handling of the final monoliths. Comparing the two shaping processes, as expected, at the same sintering temperature (1450 °C), 3D-printed substrates are better functionalized than the respective pressed samples: thus, DLP introduces desirable porosities able to enhance the functionalization. On the basis of the detailed investigation provided by the present work on the factors promoting HKUST-1 coating on mullite substrates, future work will be able to focus on the production of geometrically complex functionalized Mc and Mf monoliths and testing their $CO_2$ adsorption performance.

**Supplementary Materials:** The following supporting information can be downloaded at: https://www.mdpi.com/article/10.3390/ceramics7040114/s1, Figure S1: Mc (up) and Mf (down) mullite powders in as-received (A,D), ball-milled (B,E) and calcined (C,F) forms; Figure S2: Porosity distribution determined by MIP of Mc (a) and Mc (b) pellets sintered at 1350, 1400, 1450 and 1550 °C (respectively, black, orange and red curve); Figure S3: FESEM micrographs of HKUST-1 crystals on mullite-shaped substrates (Mc on the left and Mf on the right) sintered at 1350 °C (A,B,I,L), 1400 °C (C,D,M,N), 1450 °C (E,F,P,Q), 1550 °C (G,H,R,S).

**Author Contributions:** Conceptualization, P.P. and J.-M.T.; Methodology, B.C.; Formal analysis, A.B.; Investigation, A.B. and B.C.; Data curation, Y.M. and J.S.; Writing—original draft, A.B.; Writing—review and editing, B.C., Y.M., P.P., J.S. and J.-M.T.; Supervision, P.P. and J.-M.T. All authors have read and agreed to the published version of the manuscript.

**Funding:** This publication is part of the project NODES which has received funding from the MUR—M4C2 1.5 of PNRR funded by the European Union—NextGenerationEU (Grant agreement no. ECS00000036).

**Institutional Review Board Statement:** Not applicable.

**Informed Consent Statement:** Not applicable.

**Data Availability Statement:** The original contributions presented in the study are included in the article/supplementary material, further inquiries can be directed to the corresponding author.

**Acknowledgments:** The authors greatly acknowledge the Interdepartmental laboratory SISCON (Safety of Infrastructures and Constructions) from Politecnico di Torino for the use of the rheometer and the mercury intrusion porosimeter. Special acknowledgements to Saint-Gobain Research Provence for the supply of mullite powders.

**Conflicts of Interest:** The authors declare no conflict of interest.

## References

1. Lakhdar, Y.; Tuck, C.; Binner, J.; Terry, A.; Goodridge, R. Additive manufacturing of advanced ceramic materials. *Prog. Mater. Sci.* **2021**, *116*, 100736. [CrossRef]
2. Zocca, A.; Colombo, P.; Gomes, C.M.; Günster, J. Additive Manufacturing of Ceramics: Issues, Potentialities, and Opportunities. *J. Am. Ceram. Soc.* **2015**, *98*, 1983–2001. [CrossRef]
3. Deckers, J.; Vleugels, J.; Kruth, J.P. Additive manufacturing of ceramics: A review. *J. Ceram. Sci. Technol.* **2014**, *5*, 245–260. [CrossRef]
4. Travitzky, N.; Bonet, A.; Dermeik, B.; Fey, T.; Filbert-Demut, I.; Schlier, L.; Schlordt, T.; Greil, P. Additive manufacturing of ceramic-based materials. *Adv. Eng. Mater.* **2014**, *16*, 729–754. [CrossRef]
5. Golcha, U.; Praveen, A.S.; Belgin Paul, D.L. Direct ink writing of ceramics for bio medical applications—A Review. *IOP Conf. Ser. Mater. Sci. Eng.* **2020**, *912*, 032041. [CrossRef]
6. Lin, K.; Sheikh, R.; Romanazzo, S.; Roohani, I. 3D Printing of Bioceramic Scaffolds—Barriers to the Clinical Translation: From Promise to Reality, and Future Perspectives. *Materials* **2019**, *12*, 2660. [CrossRef]
7. Guo, W.; Li, B.; Li, P.; Zhao, L.; You, H.; Long, Y. Review on vat photopolymerization additive manufacturing of bioactive ceramic bone scaffolds. *J. Mater. Chem. B* **2023**, *11*, 9572–9596. [CrossRef]
8. Palmero, P.; Fornabaio, M.; Montanaro, L.; Reveron, H.; Esnouf, C.; Chevalier, J. Towards long lasting zirconia-based composites for dental implants. Part I: Innovative synthesis, microstructural characterization and in vitro stability. *Biomaterials* **2015**, *50*, 38–46. [CrossRef]
9. Schwarzer-Fischer, E.; Abel, J.; Sieder-Katzmann, J.; Propst, M.; Bach, C.; Scheithauer, U.; Michaelis, A. Study on CerAMfacturing of Novel Alumina Aerospike Nozzles by Lithography-Based Ceramic Vat Photopolymerization (CerAM VPP). *Materials* **2022**, *15*, 3279. [CrossRef]
10. Ding, G.; He, R.; Zhang, K.; Zhou, N.; Xu, H. Stereolithography 3D printing of SiC ceramic with potential for lightweight optical mirror. *Ceram. Int.* **2020**, *46*, 18785–18790. [CrossRef]
11. Jia, K.; Zheng, L.; Liu, W.; Zhang, J.; Yu, F.; Meng, X.; Li, C.; Sunarso, J.; Yang, N. A new and simple way to prepare monolithic solid oxide fuel cell stack by stereolithography 3D printing technology using 8 mol% yttria stabilized zirconia photocurable slurry. *J. Eur. Ceram. Soc.* **2022**, *42*, 4275–4285. [CrossRef]

12. Milovanov, Y.; Bertero, A.; Coppola, B.; Palmero, P.; Tulliani, J.-M. Mullite 3D Printed Humidity Sensors. *Ceramics* **2024**, *7*, 807–820. [CrossRef]
13. Chen, Z.; Song, X.; Lei, L.; Chen, X.; Fei, C.; Chiu, C.T.; Qian, X.; Ma, T.; Yang, Y.; Shung, K.; et al. 3D printing of piezoelectric element for energy focusing and ultrasonic sensing. *Nano Energy* **2016**, *27*, 78–86. [CrossRef]
14. Chen, Y.; Wang, N.; Ola, O.; Xia, Y.; Zhu, Y. Porous ceramics: Light in weight but heavy in energy and environment technologies. *Mater. Sci. Eng. R Rep.* **2021**, *143*, 100589. [CrossRef]
15. Santoliquido, O.; Bianchi, G.; Eggenschwiler, P.D.; Ortona, A. Additive manufacturing of periodic ceramic substrates for automotive catalyst supports. *Appl. Ceram. Technol.* **2017**, *14*, 1164–1173. [CrossRef]
16. Santoliquido, O.; Camerota, F.; Pelanconi, M.; Ferri, D.; Elsener, M.; Dimopoulos Eggenschwiler, P.; Ortona, A. Structured alumina substrates for environmental catalysis produced by stereolithography. *Appl. Sci.* **2021**, *11*, 8239. [CrossRef]
17. Pagac, M.; Hajnys, J.; Ma, Q.P.; Jancar, L.; Jansa, J.; Stefek, P.; Mesicek, J. A Review of Vat Photopolymerization Technology: Materials, Applications, Challenges, and Future Trends of 3D Printing. *Polymers* **2021**, *13*, 598. [CrossRef]
18. Suryatal, B.K.; Sarawade, S.S.; Deshmukh, S.P. Process parameter's characterization and optimization of DLP-based stereolithography system. *Prog. Addit. Manuf.* **2023**, *8*, 649–666. [CrossRef]
19. Mamatha, S.; Biswas, P.; Johnson, R. Digital light processing of ceramics: An overview on process, materials and challenges. *Prog. Addit. Manuf.* **2023**, *8*, 1083–1102. [CrossRef]
20. Fiume, E.; Coppola, B.; Montanaro, L.; Palmero, P. Vat-photopolymerization of ceramic materials: Exploring current applications in advanced multidisciplinary fields. *Front. Mater.* **2023**, *10*, 1242480. [CrossRef]
21. Kim, I.; Andreu, A.; Yoon, Y.J. A digital light processing 3D printing approach for tuning the interfacial properties of pore forming agents for porous ceramics. *Mater. Des.* **2023**, *233*, 112247. [CrossRef]
22. International Energy Agency. Technology Perspectives Energy Special Report on Carbon Capture Utilisation and Storage CCUS in Clean Energy Transitions. Available online: https://www.iea.org/reports/ccus-in-clean-energy-transitions/ (accessed on 20 November 2024).
23. Ghanbari, T.; Abnisa, F.; Wan Daud, W.M.A. A review on production of metal organic frameworks (MOF) for $CO_2$ adsorption. *Sci. Total Environ.* **2020**, *707*, 135090. [CrossRef]
24. Millward, A.R.; Yaghi, O.M. Metal-organic frameworks with exceptionally high capacity for storage of carbon dioxide at room temperature. *J. Am. Chem. Soc.* **2005**, *127*, 17998–17999. [CrossRef]
25. Moellmer, J.; Moeller, A.; Dreisbach, F.; Glaeser, R.; Staudt, R. High pressure adsorption of hydrogen, nitrogen, carbon dioxide and methane on the metal-organic framework HKUST-1. *Microporous Mesoporous Mater.* **2011**, *138*, 140–148. [CrossRef]
26. Yang, Q.; Zhong, C. Molecular simulation of carbon dioxide/methane/hydrogen mixture adsorption in metal-organic frameworks. *J. Phys. Chem. B* **2006**, *110*, 17776–17783. [CrossRef]
27. Reddy, M.S.B.; Ponnamma, D.; Sadasivuni, K.K.; Kumar, B.; Abdullah, A.M. Carbon dioxide adsorption based on porous materials. *RSC Adv.* **2021**, *11*, 12658–12681. [CrossRef]
28. Sun, J.; Shang, M.; Zhang, M.; Yu, S.; Yuan, Z.; Yi, X.; Filatov, S.; Zhang, J. Konjac glucomannan/cellulose nanofibers composite aerogel supported HKUST-1 for $CO_2$ adsorption. *Carbohydr. Polym.* **2022**, *293*, 119720. [CrossRef]
29. Park, S.; Ryu, J.; Cho, H.Y.; Sohn, D. Colloids and Surfaces A: Physicochemical and Engineering Aspects Halloysite nanotubes loaded with HKUST-1 for $CO_2$ adsorption. *Colloids Surf. A Physicochem. Eng. Asp.* **2022**, *651*, 129750. [CrossRef]
30. Cortés-Súarez, J.; Celis-Arias, V.; Beltrán, H.I.; Tejeda-Cruz, A.; Ibarra, I.A.; Romero-Ibarra, J.E.; Sánchez-González, E.; Loera-Serna, S. Synthesis and Characterization of an SWCNT@HKUST-1 Composite: Enhancing the $CO_2$ Adsorption Properties of HKUST-1. *ACS Omega* **2019**, *4*, 5275–5282. [CrossRef]
31. Xu, F.; Yu, Y.; Yan, J.; Xia, Q.; Wang, H.; Li, J.; Li, Z. Ultrafast room temperature synthesis of GrO@HKUST-1 composites with high $CO_2$ adsorption capacity and $CO_2/N_2$ adsorption selectivity. *Chem. Eng. J.* **2016**, *303*, 231–237. [CrossRef]
32. Al-Janabi, N.; Hill, P.; Torrente-Murciano, L.; Garforth, A.; Gorgojo, P.; Siperstein, F.; Fan, X. Mapping the Cu-BTC metal-organic framework (HKUST-1) stability envelope in the presence of water vapour for $CO_2$ adsorption from flue gases. *Chem. Eng. J.* **2015**, *281*, 669–677. [CrossRef]
33. Yan, X.; Komarneni, S.; Zhang, Z.; Yan, Z. Extremely enhanced $CO_2$ uptake by HKUST-1 metal-organic framework via a simple chemical treatment. *Microporous Mesoporous Mater.* **2014**, *183*, 69–73. [CrossRef]
34. Ye, S.; Jiang, X.; Ruan, L.W.; Liu, B.; Wang, Y.M.; Zhu, J.F.; Qiu, L.G. Post-combustion $CO_2$ capture with the HKUST-1 and MIL-101(Cr) metal-organic frameworks: Adsorption, separation and regeneration investigations. *Microporous Mesoporous Mater.* **2013**, *179*, 191–197. [CrossRef]
35. Liu, J.; Wang, Y.; Benin, A.I.; Jakubczak, P.; Willis, R.R.; LeVan, M.D. $CO_2/H_2O$ adsorption equilibrium and rates on metal-organic frameworks: HKUST-1 and Ni/DOBDC. *Langmuir* **2010**, *26*, 14301–14307. [CrossRef]
36. Wang, X.; Zhang, Z.; Huang, W.; Li, X.; Yan, B. Preparation of highly water stable HKUST-1@Pyr composites for excellent $CO_2$ capture capability and efficient separation of $CO_2/N_2$. *Inorg. Chem. Commun.* **2023**, *156*, 111252. [CrossRef]
37. Chen, Y.; Mu, X.; Lester, E.; Wu, T. High efficiency synthesis of HKUST-1 under mild conditions with high BET surface area and $CO_2$ uptake capacity. *Prog. Nat. Sci. Mater. Int.* **2018**, *28*, 584–589. [CrossRef]

38. Lin, K.S.; Adhikari, A.K.; Ku, C.N.; Chiang, C.L.; Kuo, H. Synthesis and characterization of porous HKUST-1 metal organic frameworks for hydrogen storage. *Int. J. Hydrogen Energy* **2012**, *37*, 13865–13871. [CrossRef]
39. Prestipino, C.; Regli, L.; Vitillo, J.G.; Bonino, F.; Damin, A.; Lamberti, C.; Zecchina, A.; Solari, P.L.; Kongshaug, K.O.; Bordiga, S. Local structure of framework Cu(II) in HKUST-1 metallorganic framework: Spectroscopic characterization upon activation and interaction with adsorbates. *Chem. Mater.* **2006**, *18*, 1337–1346. [CrossRef]
40. Wang, Z.; Liu, L.; Li, Z.; Goyal, N.; Du, T.; He, J.; Li, G.K. Shaping of Metal-Organic Frameworks: A Review. *Energy Fuels* **2022**, *36*, 2927–2944. [CrossRef]
41. Küsgens, P.; Zgaverdea, A.; Fritz, H.G.; Siegle, S.; Kaskel, S. Metal-organic frameworks in monolithic structures. *J. Am. Ceram. Soc.* **2010**, *93*, 2476–2479. [CrossRef]
42. Liu, Y.; Ng, Z.; Khan, E.A.; Jeong, H.K.; Ching, C.B.; Lai, Z. Synthesis of continuous MOF-5 membranes on porous α-alumina substrates. *Microporous Mesoporous Mater.* **2009**, *118*, 296–301. [CrossRef]
43. Lawson, S.; Hajari, A.; Rownaghi, A.A.; Rezaei, F. MOF immobilization on the surface of polymer-cordierite composite monoliths through in-situ crystal growth. *Sep. Purif. Technol.* **2017**, *183*, 173–180. [CrossRef]
44. Torrez-Herrera, J.J.; Korili, S.A.; Gil, A. Development of ceramic-MOF filters from aluminum saline slags for capturing $CO_2$. *Powder Technol.* **2023**, *429*, 118962. [CrossRef]
45. Fijoł, N.; Mautner, A.; Grape, E.S.; Bacsik, Z.; Inge, A.K.; Mathew, A.P. MOF@Cell: 3D printed biobased filters anchored with a green metal-organic framework for effluent treatment. *J. Mater. Chem. A Mater.* **2023**, *11*, 12384–12394. [CrossRef]
46. Fei, L.; Shen, L.; Chen, C.; Xu, J.; Wang, B.; Li, B.; Lin, H. Assembling 99% MOFs into Bioinspired Rigid-Flexible Coupled Membrane with Significant Permeability: The Impacts of Defects. *Small* **2024**, *20*, 2306528. [CrossRef]
47. Bertero, A.; Schmitt, J.; Kaper, H.; Coppola, B.; Palmero, P.; Tulliani, J.-M. MOFs functionalization of 3D printed mullite complex architectures for $CO_2$ capture. *Appl. Mater. Today* **2024**, *40*, 102407. [CrossRef]
48. Arnold, M.; Kortunov, P.; Jones, D.J.; Nedellec, Y.; Kärger, J.; Caro, J. Oriented crystallisation on supports and anisotropic mass transport of the metal-organic framework manganese formate. *Eur. J. Inorg. Chem.* **2007**, 60–64. [CrossRef]
49. Thomas, N.; Sreedhar, N.; Al-Ketan, O.; Rowshan, R.; Al-Rub, R.K.A.; Arafat, H. 3D printed triply periodic minimal surfaces as spacers for enhanced heat and mass transfer in membrane distillation. *Desalination* **2018**, *443*, 256–271. [CrossRef]
50. Bai, L.; Gong, C.; Chen, X.; Sun, Y.; Xin, L.; Pu, H.; Peng, Y.; Luo, J. Mechanical properties and energy absorption capabilities of functionally graded lattice structures: Experiments and simulations. *Int. J. Mech. Sci.* **2020**, *182*, 105735. [CrossRef]
51. Montazerian, H.; Mohamed, M.G.A.; Montazeri, M.M.; Kheiri, S.; Milani, A.S.; Kim, K.; Hoorfar, M. Permeability and mechanical properties of gradient porous PDMS scaffolds fabricated by 3D-printed sacrificial templates designed with minimal surfaces. *Acta Biomater.* **2019**, *96*, 149–160. [CrossRef]
52. Montazerian, H.; Zhianmanesh, M.; Davoodi, E.; Milani, A.S.; Hoorfar, M. Longitudinal and radial permeability analysis of additively manufactured porous scaffolds: Effect of pore shape and porosity. *Mater. Des.* **2017**, *122*, 146–156. [CrossRef]
53. Li, S.; Sun, Y.J.; Wang, Z.X.; Jin, C.G.; Yin, M.J.; An, Q.F. Rapid Fabrication of High-Permeability Mixed Matrix Membranes at Mild Condition for $CO_2$ Capture. *Small* **2023**, *19*, 2208177. [CrossRef] [PubMed]
54. Castro, A.P.G.; Pires, T.; Santos, J.E.; Gouveia, B.P.; Fernandes, P.R. Permeability versus design in TPMS scaffolds. *Materials* **2019**, *12*, 1313. [CrossRef] [PubMed]
55. Lima, L.K.S.; Silva, K.R.; Menezes, R.R.; Santana, L.N.L.; Lira, H.L. Microstructural characteristics, properties, synthesis and applications of mullite: A review. *Ceramica* **2022**, *68*, 126–142. [CrossRef]
56. Salomão, R.; Fernandes, L.; Spera, N.C.M. Combined effects of SiO2 ratio and purity on physical properties and microstructure of in situ alumina-mullite ceramic. *Int. J. Appl. Ceram. Technol.* **2021**, *18*, 1702–1709. [CrossRef]
57. Schneider, H.; Fischer, R.X.; Schreuer, J. Mullite: Crystal Structure and Related Properties. *J. Am. Ceram. Soc.* **2015**, *98*, 2948–2967. [CrossRef]
58. Saruhan, B.; Albers, W.; Schneider, H.; Kaysser, W.A. Reaction and Sintering Mechanisms of Mullite in the Systems Cristobalite/α-$Al_2O_3$ and Amorphous $SiO_2$/α-$Al_2O_3$. *J. Eur. Ceram. Soc.* **1996**, *16*, 1075–1081. [CrossRef]
59. de Camargo, I.L.; Erbereli, R.; Lovo, J.F.P.; Fortulan, R.; Fortulan, C.A. Digital light processing additive manufacturing of in situ mullite-zirconia composites. *J. Eur. Ceram. Soc.* **2022**, *42*, 6025–6032. [CrossRef]
60. de Camargo, I.L.; Erbereli, R.; Fortulan, C.A. Additive manufacturing of electrofused mullite slurry by digital light processing. *J. Eur. Ceram. Soc.* **2021**, *41*, 7182–7188. [CrossRef]
61. He, C.; Liu, X.; Ma, C.; Li, X.; Hou, F.; Yan, L.; Guo, A.; Liu, J. Digital light processing fabrication of mullite component derived from preceramic precusor using photosensitive hydroxysiloxane as the matrix and alumina nanoparticles as the filler. *J. Eur. Ceram. Soc.* **2021**, *41*, 5570–5577. [CrossRef]
62. Schmidt, J.; Altun, A.A.; Schwentenwein, M.; Colombo, P. Complex mullite structures fabricated via digital light processing of a preceramic polysiloxane with active alumina fillers. *J. Eur. Ceram. Soc.* **2019**, *39*, 1336–1343. [CrossRef]

63. Lee, R.-T.; Cheng, W.-S.; Lee, C.-S.; Lin, F.-F.; Liu, F.-H. Mullite Ceramic Fabrication by 3D Printing. In Proceedings of the 7th International Conference on Mechanics and Materials in Design, Albufeira, Portugal, 11–15 June 2017.
64. Rezaei, F.; Lawson, S.; Hosseini, H.; Thakkar, H.; Hajari, A.; Monjezi, S.; Rownaghi, A.A. MOF-74 and UTSA-16 film growth on monolithic structures and their $CO_2$ adsorption performance MOF-74 and UTSA-16 film growth on monolithic structures and their $CO_2$ adsorption performance. *Chem. Eng. J.* **2017**, *313*, 1346–1353. [CrossRef]
65. Gascon, J.; Aguado, S.; Kapteijn, F. Manufacture of dense coatings of $Cu_3(BTC)_2$ (HKUST-1) on α-alumina. *Microporous Mesoporous Mater.* **2008**, *113*, 132–138. [CrossRef]
66. Hermes, S.; Schröder, F.; Chelmowski, R.; Wöll, C.; Fischer, R.A. Selective nucleation and growth of metal-organic open framework thin films on patterned COOH/$CF_3$-terminated self-assembled monolayers on Au(111). *J. Am. Chem. Soc.* **2005**, *127*, 13744–13745. [CrossRef]
67. Huang, A.; Dou, W.; Caro, J. Steam-stable zeolitic imidazolate framework ZIF-90 membrane with hydrogen selectivity through covalent functionalization. *J. Am. Chem. Soc.* **2010**, *132*, 15562–15564. [CrossRef]
68. Synthetic Mullite. 2024. Available online: https://www.itc-cera.co.jp/english/prod/prod04.html (accessed on 20 November 2024).
69. Sintered Mullite—Jiangsu Jingxin New Materials Co., Ltd. Available online: https://www.jxrefractory.com/product/sintered-mullite.html (accessed on 23 September 2024).
70. Montanaro, L.; Tulliani, J.M.; Perrot, C.; Negro, A. Sintering of Industrial Mullites. *J. Eur. Ceram. Soc.* **1997**, *11*, 1715–1723. [CrossRef]
71. Gabdullin, A.N.; Molodykh, A.S.; Nikonenko, E.A.; Nikitina, E.V.; Tkacheva, V.E.; Nevolina, O.A. High-temperature hydrolysis of magnesium nitrate hexahydrate. *Russ. Metall.* **2017**, *2017*, 627–630. [CrossRef]
72. Yu, P.C.; Tsai, Y.W.; Yen, F.S.; Huang, C.L. Thermal reaction of cristobalite in nano- SiO2/α- Al 2 O3 powder systems for mullite synthesis. *J. Am. Ceram. Soc.* **2014**, *97*, 2431–2438. [CrossRef]
73. Skinner, K.G.; Cook, W.H.; Potter, R.A.; Palmour, H. Effect of $TiO_2$, $Fe_2O_3$, and Alkali on Mineralogical and Physical Properties of Mullite-Type and Mullite-Forming $Al_2O_3$-$SiO_2$ Mixtures: I. *J. Am. Ceram. Soc.* **1953**, *36*, 349–356. [CrossRef]
74. de Camargo, I.L.; Morais, M.M.; Fortulan, C.A.; Branciforti, M.C. A review on the rheological behavior and formulations of ceramic suspensions for vat photopolymerization. *Ceram. Int.* **2021**, *47*, 11906–11921. [CrossRef]
75. Chapter 1—Non-Newtonian fluid behaviour. In *Non-Newtonian Flow and Applied Rheology: Engineering Applications*; Elsevier: Amsterdam, The Netherlands, 2008; pp. 1–55. [CrossRef]
76. Tangsathitkulchai, C.; Austin, L.G. Rheology of Concentrated Slurries of Particles of Natural Size Distribution Produced by Grinding. *Powder Technol.* **1988**, *56*, 293–299. [CrossRef]
77. Senapati, P.K.; Panda, D.; Parida, A. Predicting Viscosity of Limestone-Water Slurry. *J. Miner. Mater. Charact. Eng.* **2009**, *8*, 203–221. [CrossRef]
78. Olhero, S.M.; Ferreira, J.M.F. Influence of particle size distribution on rheology and particle packing of silica-based suspensions. *Powder Technol.* **2004**, *139*, 69–75. [CrossRef]
79. Diptanshu; Miao, G.; Ma, C. Vat photopolymerization 3D printing of ceramics: Effects of fine powder. *Manuf. Lett.* **2019**, *21*, 20–23. [CrossRef]
80. Lestari, W.W.; Adreane, M.; Purnawan, C.; Fansuri, H.; Widiastuti, N.; Rahardjo, S.B. Solvothermal and electrochemical synthetic method of HKUST-1 and its methane storage capacity. *IOP Conf. Ser. Mater. Sci. Eng.* **2016**, *107*, 012030. [CrossRef]
81. Gao, W.Y.; Leng, K.; Cash, L.; Chrzanowski, M.; Stackhouse, C.A.; Sun, Y.; Ma, S. Investigation of prototypal MOFs consisting of polyhedral cages with accessible Lewis-acid sites for quinoline synthesis. *Chem. Commun.* **2015**, *51*, 4827–4829. [CrossRef]
82. Hartmann, M.; Kunz, S.; Himsl, D.; Tangermann, O.; Ernst, S.; Wagener, A. Adsorptive separation of isobutene and isobutane on $Cu_3(BTC)_2$. *Langmuir* **2008**, *24*, 8634–8642. [CrossRef]
83. Schlichte, K.; Kratzke, T.; Kaskel, S. Improved synthesis, thermal stability and catalytic properties of the metal-organic framework compound $Cu_3(BTC)_2$. *Microporous Mesoporous Mater.* **2004**, *73*, 81–88. [CrossRef]
84. Ni, Z.; Masel, R.I. Rapid production of metal-organic frameworks via microwave-assisted solvothermal synthesis. *J. Am. Chem. Soc.* **2006**, *128*, 12394–12395. [CrossRef]
85. Ryan, T. The Development of Instrumentation for Thin-Film X-ray Diffraction. *J. Chem. Educ.* **2001**, *78*, 613–616. [CrossRef]
86. Masiello, F.; Fransen, M. Benefits of Hard X-Radiation White Paper. Available online: https://www.malvernpanalytical.com/en/assets/white%20paper%20benefits%20of%20hard%20x-radiation_tcm50-46028.pdf (accessed on 20 November 2024).
87. Janeba, D.; Čapková, P.; Weiss, Z.; Schenk, H. XRD Profile Analysis of Clay Minerals. *Mater. Sci. Forum* **1998**, *278–281*, 139–144. [CrossRef]
88. Zhu, M.; Tian, P.; Kurtz, R.; Lunkenbein, T.; Xu, J.; Schlögl, R.; Wachs, I.E.; Han, Y.F. Strong Metal–Support Interactions between Copper and Iron Oxide during the High-Temperature Water-Gas Shift Reaction. *Angew. Chem. Int. Ed.* **2019**, *58*, 9083–9087. [CrossRef] [PubMed]

89. Yao, X.; Ma, X.; Gao, X.; Jia, L. Preparation of magnetic metal organic framework nanocomposites for efficient and selective adsorption of hemoglobin from bovine blood. *RSC Adv.* **2017**, *7*, 29330–29338. [CrossRef]
90. Niu, H.; Liu, P.; Qin, F.; Liu, X.L.; Akinay, Y. PEDOT coated Cu-BTC metal-organic frameworks decorated with Fe3O4 nanoparticles and their enhanced electromagnetic wave absorption. *Mater. Chem. Phys.* **2020**, *253*, 123458. [CrossRef]